3-2021

A Comparison of Sporadic-E Occurrence Rates Using Ionosondes and GPS Radio Occultation Measurements

Rodney A. Carmona Jr.

A Comparison of Sporadic-E Occurrence Rates
Using Ionosonde and GPS Radio Occultation
Measurements

THESIS

Rodney Alan Carmona Jr, 1st Lt, USAF

AFIT-ENP-MS-21-M-108

DEPARTMENT OF THE AIR FORCE
AIR UNIVERSITY

AIR FORCE INSTITUTE OF TECHNOLOGY

Wright-Patterson Air Force Base, Ohio

A COMPARISON OF SPORADIC-E OCCURRENCE

RATES USING IONOSONDE AND

GPS RADIO OCCULTATION MEASUREMENTS

THESIS

Presented to the Faculty

Department of Engineering Physics

Graduate School of Engineering and Management

Air Force Institute of Technology

Air University

Air Education and Training Command

in Partial Fulfillment of the Requirements for the

Degree of Master of Science in Applied Physics

Rodney Alan Carmona Jr, B.S.

1st Lt, USAF

March 2021

AFIT-ENP-MS-21-M-108

A COMPARISON OF SPORADIC-E OCCURRENCE

RATES USING IONOSONDE AND

GPS RADIO OCCULTATION MEASUREMENTS

THESIS

Rodney Alan Carmona Jr, B.S.
1st Lt, USAF

Committee Membership:

Maj Daniel J. Emmons, Ph.D.
Chair

Dr. Eugene V. Dao
Member

Lt Col Omar A. Nava, Ph.D.
Member

AFIT-ENP-MS-21-M-108

Abstract

Sporadic-E (E_s) occurrence rates from Global Position Satellite radio occultation (GPS-RO) measurements have shown to vary by nearly an order of magnitude between studies, motivating a comparison with ground-based measurements. In an attempt to find an accurate GPS-RO technique for detecting E_s formation, occurrence rates derived using five previously developed GPS-RO techniques are compared to ionosonde measurements over an eight-year period from 2010-2017. GPS-RO measurements within 170 km of a ionosonde site are used to calculate E_s occurrence rates and compared to the ground-truth ionosonde measurements. Each technique is compared individually for each ionosonde site and then combined to determine the most accurate GPS-RO technique for binary (present or absent) E_s measurements. Overall, the Yu et al. (2020) S_4 method showed the closest agreement with ionosonde measurements between 2010-2017 and is the recommended technique for future GPS-RO based E_s climatologies.

Acknowledgements

I would like to thank my family to have the patience to support me through this program.

I would like to thank Maj Dan Emmons, my thesis advisor, for assisting me in overcoming my faults and enhancing strengths. His mentor-ship has helped me become a better researcher and scholar.

I would also like to thank Dawn K. Merriman, her efforts has led to the success of this project and I am in her debt.

I would also like to thank my committee members, Lt Col Omar A. Nava and Dr. Eugene V. Dao

Rodney Alan Carmona Jr

Table of Contents

List of Figures

List of Tables

I. Introduction

Ionospheric conditions are important to a range of electromagnetic spectrum operations (EMSO), such as the function of satellite and high frequency (HF) communications. Abnormalities such as sporadic-E (E_s) can cause degradation of the communication signals as well reflect it entirely (Arras and Wickert, 2018; Chu et al., 2014; Denardini et al., 2016). Department of Defense surveillance techniques such as over-the-horizon-radar and HF geolocation are also significantly affected by the presence of sporadic-E, motivating the need for accurate, real-time, global sporadic-E observations.

Sporadic-E manifests itself as a non-uniform, wavy layer, or a composition of irregular elongated clouds of intense ionization within the lower E-region of the ionosphere (Zeng and Sokolovskiy, 2010). Real-time observation of the ionosphere is conducted globally with ground-based ionosonde stations, incoherent-scatter radars, and very high frequency radar (Niu et al., 2019). These devices use radio signals to probe the ionosphere and measure plasma parameters (Hajj and Romans, 1998). However, the limitations in power and quantity of sites have made this task difficult (Igarashi et al., 2001).

The limited number of ground-based observations are insufficient to provide an accurate picture of the global ionospheric conditions, which also requires a space based approach. The Constellation Observing Satellite for Meteorology, Ionosphere, and Climate (COSMIC) uses methods to find abnormalities in the ionosphere through a measurement techniques known as Global Position Satellite (GPS) radio occultation. This constellation of six satellites monitors conditions of the Earth's ionosphere and neutral atmosphere (Chu et al., 2010; Resources, 2014; Rocken et al., 2000).

The COSMIC constellations use GPS signals for radio occultation (GPS-RO) measurements (Resources, 2014). COSMIC specifications include circular orbits at alti-

tudes of 800 km with an inclination of 72 degrees, providing an average of 1,500-2,000 GPS-RO profiles per day (Resources, 2014; Rocken et al., 2000). By using the COSMIC constellations to receive dual L_1 (1575.42 MHz) and L_2 (1227.60 MHz) radio signals that propagate through the ionosphere from the GPS satellites, the signal perturbation caused by a sporadic-E layer can be measured (Chu et al., 2010; Ware et al., 2000). This method can also be used to find temperature, water vapor pressure, and ionospheric electron density (Chu et al., 2010; Kursinski et al., 2000). The COSMIC-1 constellation is currently being succeeded by the COSMIC-2 constellation which increases the frequency and range of the sensors activity (Satellite and Service, 2020). Using the data collected from both of these constellations and pairing it with the ground based information enhances characterization of the ionosphere.

The primary motivation behind this project are the large discrepancies in occurrence rates between different GPS-RO methods for locating sporadic-E. For example, the Chu et al. (2014) method shows a maximum of 10% occurrence rate while Arras and Wickert (2018) presents a 40-50% maximum. These discrepancies require a comparison against reliable methods such as ionosonde based E_s measurements.

To find an accurate GPS-RO method for monitoring sporadic-E, five GPS-RO techniques are compared to ionosonde measurements over an eight year period between 2010-2017. The Arras and Wickert (2018) technique uses the Signal-to-Noise Ratio (SNR) profiles of the GPS L_1 signal to calculate a standard deviation to compare against an empirically determined threshold. Chu et al. (2014) uses GPS L_1 and L_2 signals to find perturbations larger than 5 cm, checks the phase ratio between L_2 and L_1, and analyzes the L_1 SNR perturbation. Niu et al. (2019) uses Total electron content (TEC) density profiles to calculate the maximum vertical gradient of the TEC perturbations. Gooch et al. (2020) detrends the TEC using a Savitsky-Golay filter and finds the electron density by computing TEC enhancement and dividing by an

effective path length. Finally, the Yu et al. (2020) technique uses the S_4 maximum, which is the standard deviation of signal intensity normalized by average intensities, to convert to a sporadic-E intensity. For this comparison, data from the digital ionosonde brand Digisonde is used as the ground-truth for sporadic-E occurrence rates across the globe.

Chapter II discusses the background of the ionosphere, sporadic-E, and measurement techniques. Chapter III provides details on GPS-RO data extractions from the COSMIC constellations and comparisons to ionosonde data with the five different methods spanning multiple years. Chapter IV presents the conclusions and provides suggestions for future work in this area.

II. Background

The purpose of this chapter is to describe the ionosphere's interaction with signals propagating from Earth and its satellites. First, sporadic-E properties and impacts are described. Second, a few types ionospheric measurements are discussed. Third, the importance of the ionosonde is explained. Finally, GPS radio occultation and its role in identifying sporadic-E are discussed.

2.1 Sporadic-E

Sporadic-E are clouds of metallic ions in the lower E-region of ionosphere at an altitude of 95-125 km (Haldoupis, 2019). The clouds typically have a large day-to-day variability and distinct features dependent on altitude of observance (Denardini et al., 2016). A narrow ionization thickness of 2-10 km in height (Denardini et al., 2016) is one distinct feature of E_s layers, and the average layer horizontal width is ~170 km (Cathey, 1969). The main physical mechanism currently applied to sporadic-E formation is the wind-shear theory using vertical shears in the zonal wind that converge the long-lived metal ions in the lower thermosphere vertically into enhanced plasma layers (Haldoupis et al., 2007; Whitehead, 1989). Atmospheric wave dynamics provide the vertical wind shears needed for ion convergence. Another element of sporadic-E variability comes from seasonal dependence that shows local summer maxima caused by seasonal variability of thermospheric meteor deposits (Haldoupis, 2011).

Sporadic-E observations are important for propagating and receiving radio signals further than line of sight, primarily in the HF 3-30 MHz and very high frequency (VHF) 30-100 MHz bands (Rice et al., 2011). Over-the-horizon (OTH) radar uses sky-wave propagation in the HF band by reflecting a signal off the ionosphere to detect targets at distances greater than microwave radars limited by line of sight

(Figure 1) (Headrick and Skolnik, 1974). HF geolocation uses measured sky-wave signals to estimate an unknown transmitter's position by backtracking the signal from the receive location through the ionosphere down to an estimated transmit location (Fabrizio, 2014).
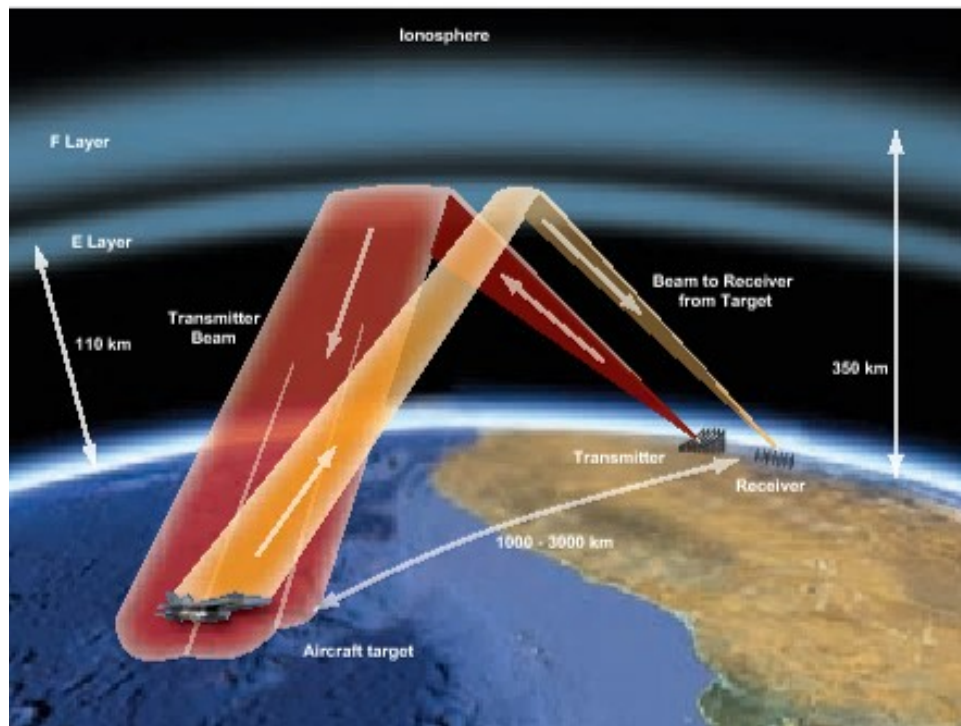
Figure 1. An example of Over-the-Horizon radar sky-wave propagation to locate objects of interest (Fabrizio, 2014).

Possessing a greater understanding and method of measuring sporadic-E will allow detection in locations where ionosonde sites are not feasible or permitted, such as the oceans. Additionally, the nearly global coverage of GPS-RO measurements can improve sporadic-E climatologies with limited measurement locations, such as the widely used sporadic-E occurrence rate climatology developed by Smith (1957). As displayed in Figure 2, the sparsity of ground-based measurement sites forces interpolation over vast distances, which may provide occurrence rates that do not correspond

to reality.
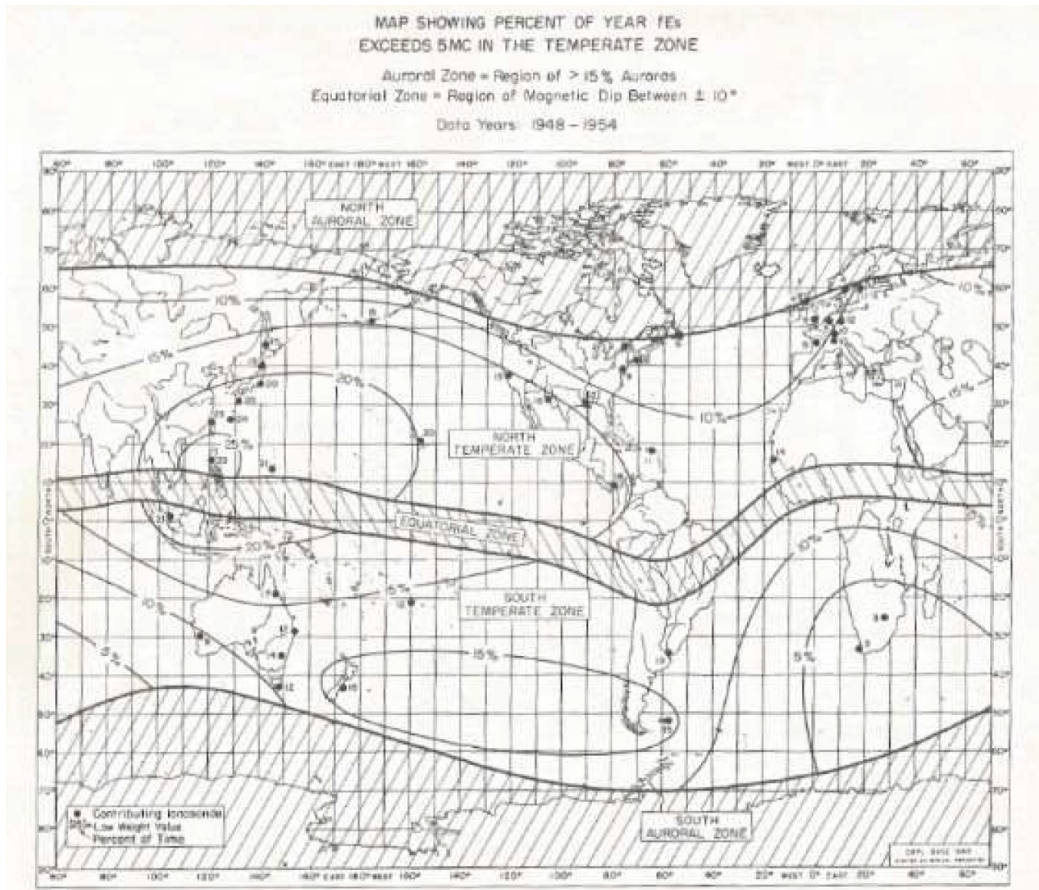
Figure 2. An example of 1948 - 1954 Map showing Sporadic-E Rates as well as the areas not covered in that time period (Smith, 1957).

2.2 Ionosphere Measurements

There are two overarching methods for extracting sporadic-E parameters from GPS-RO measurements: phase perturbation (TEC) or signal amplitude (diffraction) analysis. The S index is a measured the vertical TEC gradient, while the S_4 index provides a measure of amplitude perturbations and diffraction. TEC is calculated by receiving L_1 ($f_1 = 1.57542$ GHz) and L_2 ($f_2 = 1.22760$ GHz) signals aboard a low earth orbit satellite and using the excess phase (ΔL_1 and ΔL_2) in the equation

6

(Igarashi et al., 2001):

$$TEC = \frac{1}{40.3} \frac{f_1^2 f_2^2}{f_1^2 - f_2^2} (\Delta L_1 - \Delta L_2). \tag{1}$$

The S index profile is defined as the vertical gradient of the detrended TEC (ΔTEC) to estimate sporadic-E intensity where dh is the change in height (Niu et al., 2019):

$$S = \frac{d(\Delta TEC)}{dh}. \tag{2}$$

The S_4 index profile is defined as the standard deviation of signal intensity (SNR^2 for COSMIC measurements) fluctuations normalized by average intensities and is useful due to its linear dependence on the electron density (Briggs and Parkin, 1963; Yu et al., 2020):

$$S_4 = \sqrt{\frac{< \mathrm{SNR}^4 > - < \mathrm{SNR}^2 >^2}{< \mathrm{SNR}^2 >^2}}. \tag{3}$$

Other methods to measure the ionosphere include ionosondes, which measure propagation times for various HF frequencies to extract information on the vertical structure of the ionosphere (Figure 3). Another device to measure the ionosphere is an Incoherent Scatter Radar (ISR) which transmits a pulse in to the ionosphere where the radiation is re-radiated by the electrons through Thomson scattering and is Doppler shifted by the thermal motion of the electrons (Gordon, 1958). Using multiple pulses, an altitude can be studied with different frequencies to give an in-depth look with the different perspectives (Hargreaves, 1992). The difference between ISR and ionosondes is that ISR measures the topside of the ionosphere while the ionosondes measure the bottomside. However, ISR operation is expensive and requires a large powerful transmitter to receive the weak scatter signals (Figure 4). GPS ground based receivers also play a role in measurements by estimating the inter-frequency

7

biases and calculating the TEC through varying slices of the ionosphere. Most of the techniques applied estimate the vertical ionospheric structure (Komjathy et al., 2005).
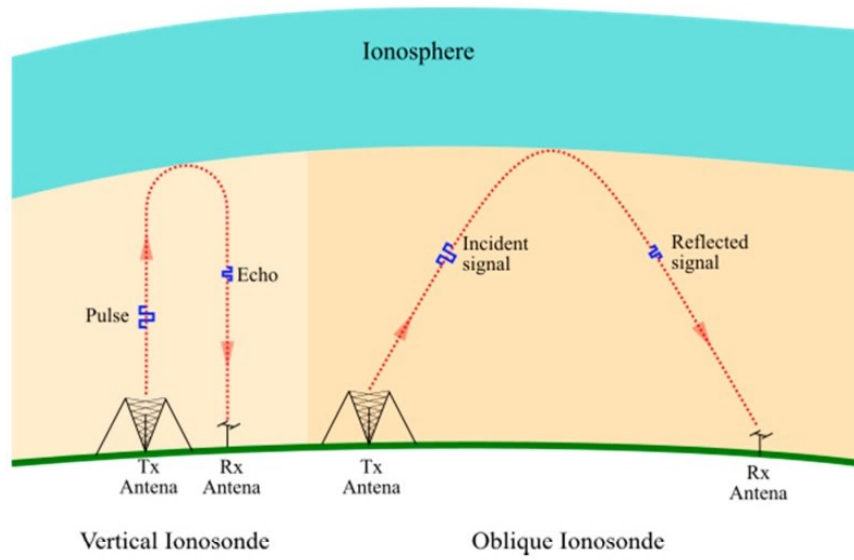
Figure 3. A diagram of vertical and oblique ionosonde operations. (Barona Mendoza et al., 2017)

Figure 4. Millstone Hill Radar from the MIT Haystack Observatory (Observatory, 2018).

2.2.1 Ionosondes

An ionosonde is a chirp machine that transmits a signal to the ionosphere and measures the propagation time after reflection from the ionosphere plasma. After sweeping through a range of frequencies, the travel time as a function of frequency is recorded and called an ionogram (Reinisch, 2019). The virtual height h' is defined by

$$h'(f) = \frac{1}{2}\tau(f)\,c, \tag{4}$$

where τ is the measured pulse travel time and c is the free speed of light (Reinisch, 2019). The dispersive nature of a plasma causes τ to be a function of signal frequency, f. This frequency dependence is exploited by ionosondes to invert the virtual height measurements to actual heights through an estimation of the bottomside electron density profiles.

There are several different types of ionosonde machines that could be used for this study, however Digisondes were used due to the long-term global data available from the Global Ionosphere Radio Observatory (GIRO) network (`http://giro.uml.edu/`) and established auto-scaling ARTIST software. A digital ionospheric sounding system developed around 1969 is the Digisonde 128PS which has two modes of operation: Ionogram Mode with full range and frequency but limited resolution and Doppler-Drift Mode with full resolution in Doppler and incidence angle but limited frequency range (Bibl and Reinisch, 1978). The Digisonde-4D (2008) offers new ways to use software such as ARTIST-5 (Galkin and Reinisch, 2008) to increase the flexibility in the measurement enhancements as well as mitigate some of the radio frequency (RF) interference (Reinisch et al., 2009). An example ionogram from Lowell DIDBase is displayed in Figure 5. The global GIRO network of Digisondes is displayed in Figure 6 along with the planned and upcoming sites to the network.
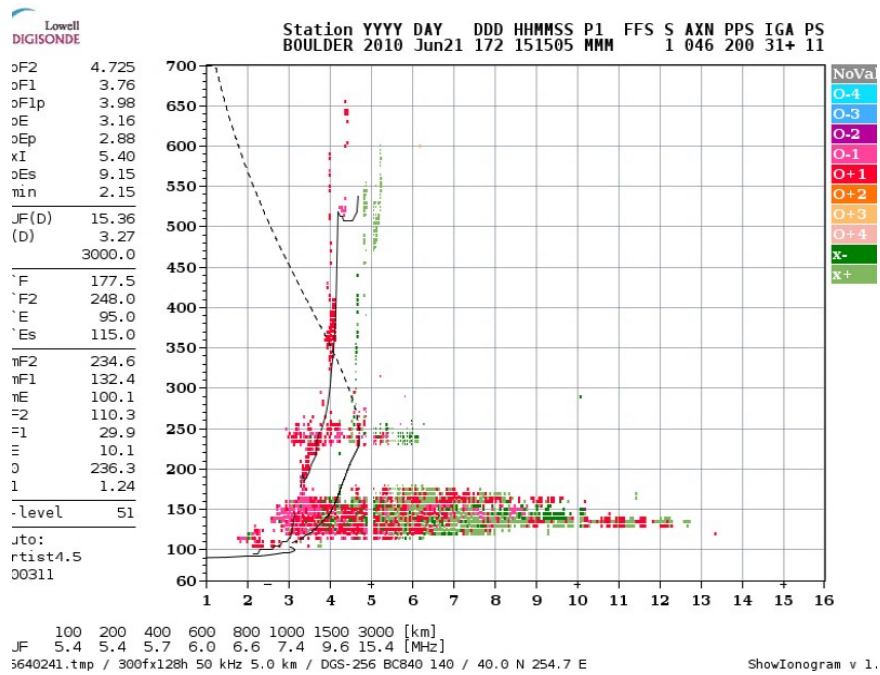
Figure 5. Ionogram from Boulder Colorado on 21 June 2010 measured by a Digisonde which shows the strong sporadic-E layer around the 100 km altitude (`https://ulcar.uml.edu/DIDBase/`).
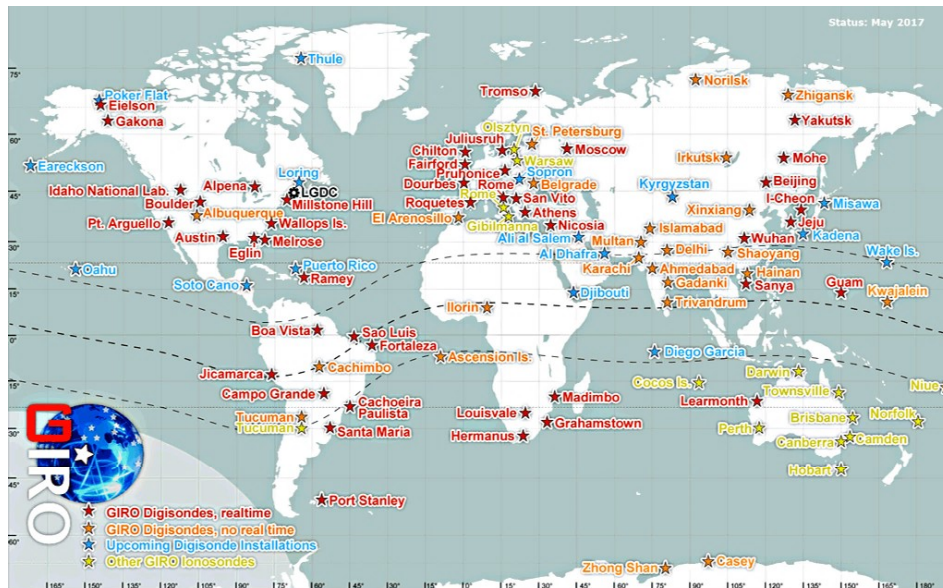
Figure 6. Map of current and upcoming Digisonde locations as of Dec 2020 (GIRO, 2018).

10

2.3 GPS Radio Occultation

In GPS radio occultation the scintillation of the radio waves is one of the most important tools to measure ionosphere irregularities (Chytil, 1967). GPS-RO consists of transmitting GPS L_1 and L_2 signals to a Low Earth Orbit (LEO) satellite and measuring the signal amplitude, phase, and Doppler shift after traversing through the Earth's atmosphere and ionosphere (Hajj and Romans, 1998). GPS radio occultation can yield approximately 500 occultations per satellite each day (Kursinski et al., 1997). A graphical illustration of the RO geometry from a GPS satellite to a COSMIC satellite is shown in Figure 7. The electron density can be obtained by measuring the phase change and amplitude fluctuation between the transmitter and receiver using principles of the index of refraction (Hajj and Romans, 1998). For high frequency signals, the index of refraction, n, can be approximated by

$$n = 1 - 40.3 \, \frac{n_e}{f^2}, \tag{5}$$

where n_e is the electron density $(1/m^3)$ and f is the signal frequency in hertz (Hajj and Romans, 1998). The phase accumulated between the satellites can be modeled by

$$\Phi = \rho + B^{transmitted} - B^{received} + \Delta^{neutral} + \Delta^{ionosphere} + b, \tag{6}$$

where ρ is the geometric range, $B^{transmitted}$ and $B^{received}$ are clock biases for transmitter and receiver, $\Delta^{neutral}$ is atmosphere delay, $\Delta^{ionosphere}$ is ionosphere delay, and b is phase ambiguity (Hajj and Romans, 1998). The $\Delta^{ionosphere}$ is an important parameter as it's the primary phase contribution as the radio-path crosses a sporadic-E layer. A characteristic u-shape is observed in SNR measurements of sporadic-E layers caused by defocusing of the signal (Zeng and Sokolovskiy, 2010). The sporadic-E layer acts like a negative lens diverging the GPS signal. Additionally, the diffraction caused by

the perturbing layer can be used to characterize the sporadic-E intensity (Arras and Wickert, 2018; Gooch et al., 2020). These fluctuations are monitored and Figure 8 shows the global COSMIC I coverage from a typical day in 2013.
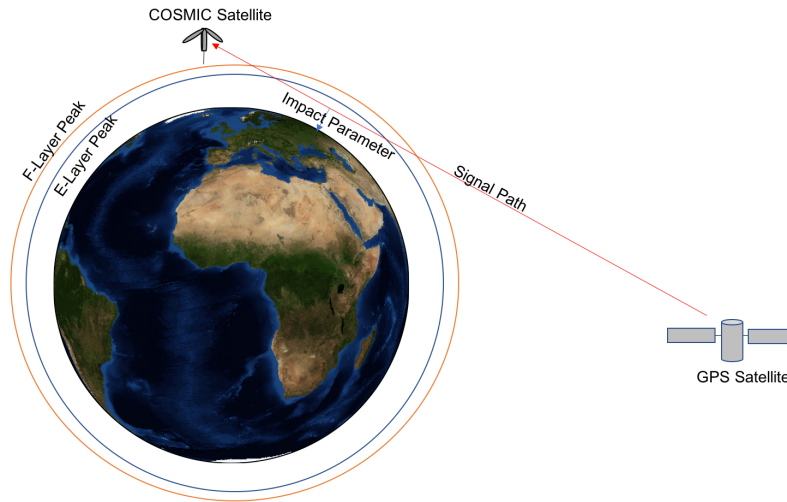
Figure 7. Illustration of the signal path between GPS and COSMIC satellites through the ionosphere (Gooch et al., 2020).
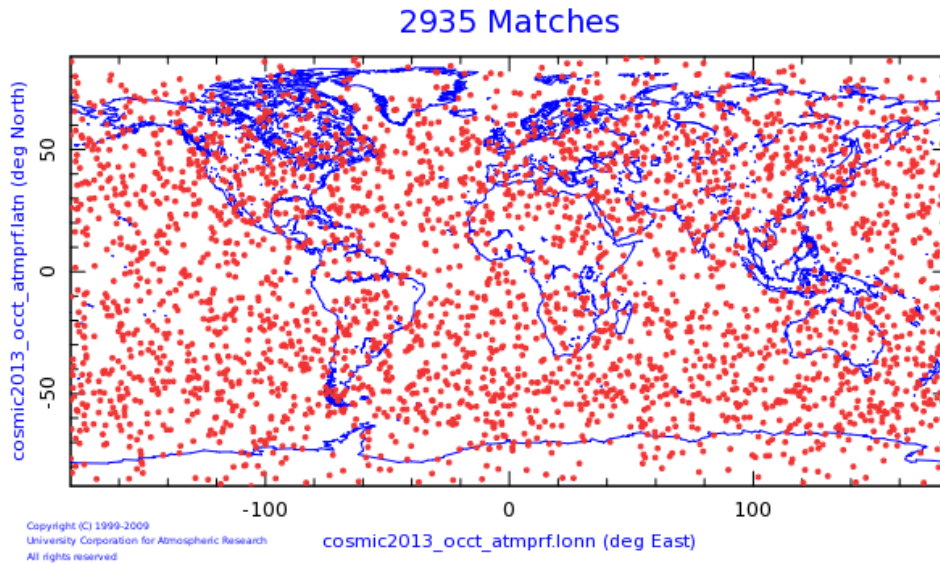
Figure 8. Global occultation map for the COSMIC I constellation on a day in 2010 (https://cdaac-www.cosmic.ucar.edu/).

III. Methodology

3.1 Data Extraction and Structuring

The COSMIC constellation provides RO data through measurements of GPS signals. This is archived through the COSMIC Data Analysis and Archive Center (CDAAC) data servers (Analysis and Center, 2021). Ignoring the minimal bending caused by the ionosphere (Schreiner et al., 1999) the signal tangent point can be calculated using a coordinate transformation from the Earth-Centered-Inertial (ECI) coordinates to latitude, longitude, and altitude implemented in Astropy (Community, 2021). The L_1 and L_2 excess phase and SNR measurements over time are assigned to this tangent point, proving an approximate measurement location to compare with ionosonde data. The GPS time is converted to Earth Fixed Time with time zones and it also accounts for leap-year.

3.2 GPS-RO Methods

Here we outline the five GPS-RO techniques used to calculate sporadic-E occurrence rates. The range of altitudes is 70-130 km following the typical sporadic-E altitude range (Arras and Wickert, 2018). For any technique without an explicit binary threshold, we use a lower fbEs threshold of 3 MHz and an upper threshold of 20 MHz to remove unrealistic or noisy data. In this study, we use foEs and fbEs interchangeably for the GPS-RO measurements as the uniform blanketing sporadic-E layers corresponding to large GPS-RO perturbations are most likely related to fbEs rather than potentially patchy foEs measurements (Arras and Wickert, 2018; Reddy and Mukunda Rao, 1968). However, the ionosonde data strictly uses fbEs instead of foEs for the comparison.

To improve readability, from here on I will refer to the methods as "Arras" for

13

Arras and Wickert (2018), "Niu" for Niu et al. (2019), "Chu" for Chu et al. (2010), "Gooch" for Gooch et al. (2020), and "Yu" for Yu et al. (2020). Table 1 provides a summary of the criteria used in each technique.

Table 1. A summary of the binary sporadic-E criteria for each of the five GPS-RO techniques.

Technique	Criteria
Arras	L_1 SNR standard deviation greater than 0.2
Niu	Maximum TEC perturbation gradient (S_{max}) greater than 0.12 TECU/km
Chu	1) L_1 and L_2 phase perturbation greater than 5 cm
	2) ratio of L_1 and L_2 within 1.5-1.8 range
	3) amplitude of normalized L_1 SNR perturbation greater than 0.01
Yu	Maximum L_1 S_4 greater than 0.66
Gooch	fbEs calculated from TEC perturbation and 170 km effective sporadic-E length greater than 3 MHz

3.2.1 Arras and Wickert (2018) method

The range of altitudes used for the Arras method is 70-130 km following the boundaries of typical sporadic-E. Within this range the 50 Hz L_1 data (atmPhs files from CDAAC) is used since the lower frequency L_2 is noisier from elevated index of refraction gradients. To search for sporadic-E, the L_1 SNR is normalized and a rolling standard deviation is calculated using a 2 km window. If the standard deviation exceeds an empirically determined value of 0.2 then the surrounding altitude is examined on both sides. With typical sporadic-E vertical thicknesses on the order of 1 km (Zeng and Sokolovskiy, 2010), if the altitude extent of the perturbed region with a standard deviation over 0.2 exceeds 10 km then the occultation is removed for

quality control. An example is displayed in Figure 9 showing sporadic-E around the 100 km height. This method was used to create a global E_s occurrence climatology separated by season. Additionally, Arras and Wickert (2018) showed that the polar rates are low compared to the mid-latitudes and that the magnetic equator held almost no sporadic-E.
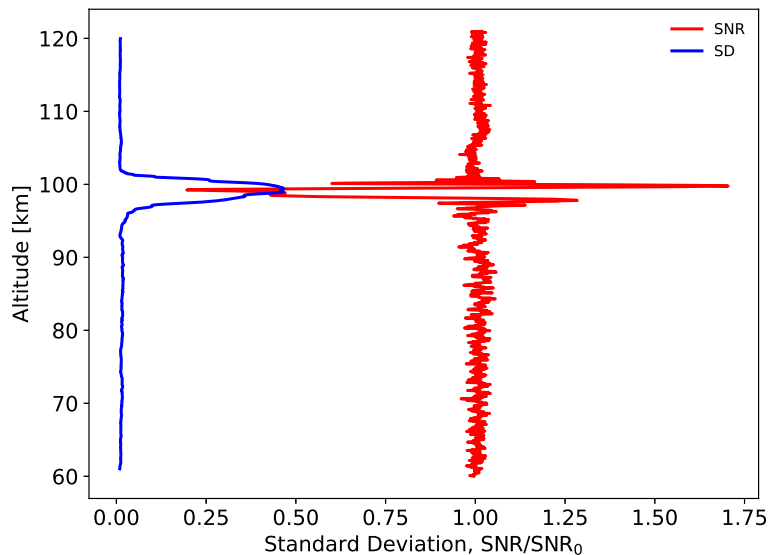
Figure 9. The normalized L_1 SNR and corresponding standard deviation.

3.2.2 Niu et al. (2019) Method

TEC profiles are calculating using L_1 and L_2 excess phase data from the 1 Hz ionPhs CDAAC files. The TEC profiles with an altitude range of 70-130 km are detrended using a Savitzky-Golay 11 point, 3rd order polynomial to obtain the background TEC profile, $TEC_{Background}$:

$$TEC_{Detrended} = TEC - TEC_{Background}, \tag{7}$$

15

where TEC is the raw TEC and $TEC_{Detrended}$ is the TEC perturbation (or detrended TEC). The S_{max} is the maximum vertical gradient of $TEC_{Detrended}$, as described in Equation 2. An example of the calculated S_{max} for a typical sporadic-E profile is displayed in Figure 10, where a sporadic-E layer is present at an altitude of $\sim$95 km. Averaging the linear fits of S_{max} as a function of foEs obtained by Niu et al. (2019) provides:

$$S_{max}\,[\mathrm{TECU/km}] = 0.0502 \times foEs\,[\mathrm{MHz}] - 0.0304. \tag{8}$$

The four slopes are averaged to give a global slope by combining the slopes found for different locations around the globe. From this averaged slope, we find a threshold S_{max} of 0.12 TECU/km corresponding to a 3 MHz foEs. Niu et al. (2019) showed that sporadic-E intensity is correlated with magnetic latitude dependency and solar activity. It also showed that seasonal variation took place more in the mid-latitude region.
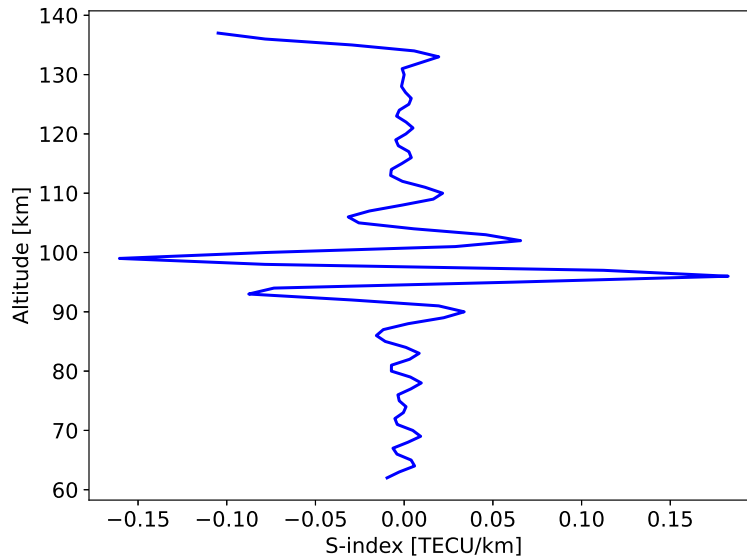
Figure 10. An example S index profile calculated as the vertical gradient of the detrended TEC ($TEC - TEC_{Background}$)**.**

3.2.3 Chu et al. (2014) Method

The 1 Hz COSMIC (ionPhs) phase and SNR data is used within an altitude of 70-130 km. This method requires three criteria to be satisfied simultaneously: First, both the L_1 and L_2 SNR and excess phase are smoothed with a 3 point Savitzky-Golay filter as displayed in Figure 11. Both the L_1 and L_2 phase perturbation magnitudes must be larger than 5 cm as in Figure 12. The excess phase on both the L_1 and L_2 are de-trended using a Savitzky-Golay filter with a 25 km window and 3rd order polynomial to remove large scale variations in the E-layer of ionosphere. The phase perturbation magnitudes, ΔL, are inversely proportional to the signal frequency squared:

$$\Delta L = \frac{40.323}{f^2} TEC. \tag{9}$$

Therefore, the ratio of $\Delta L_2 / \Delta L_1$ should have a value of 1.65 if the signals share the same group path. From this, the second criteria requires the phase perturbation ratio to lie within the range of 1.5-1.8.

Finally, the amplitude of the normalized L_1 SNR perturbation has to be greater than 0.01 as displayed in Figure 13. The height where the peak of the perturbation occurs is the height of the sporadic-E layer. Chu et al. (2010) used this method to create a global climatology that removed magnetic activity and other irregularities from the raw measurements. This study was able to show summer and winter occurrence rates of sporadic-E are likely due to the metallic ion flux.
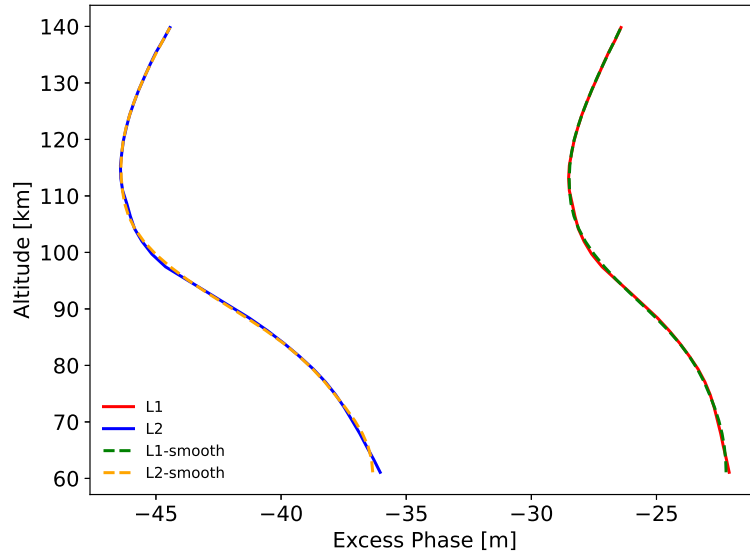
Figure 11. An example of L_1 and L_2 excess phase measurements.
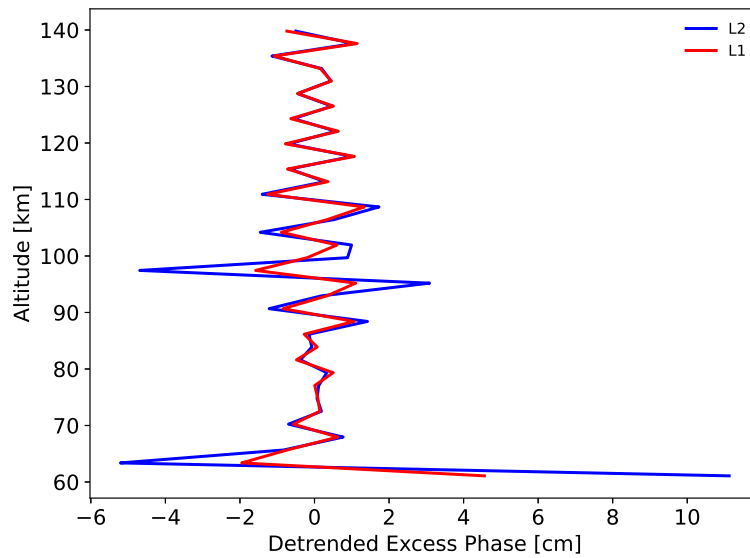
Figure 12. An example of the detrended excess phase for both the L_1 and L_2 signals.
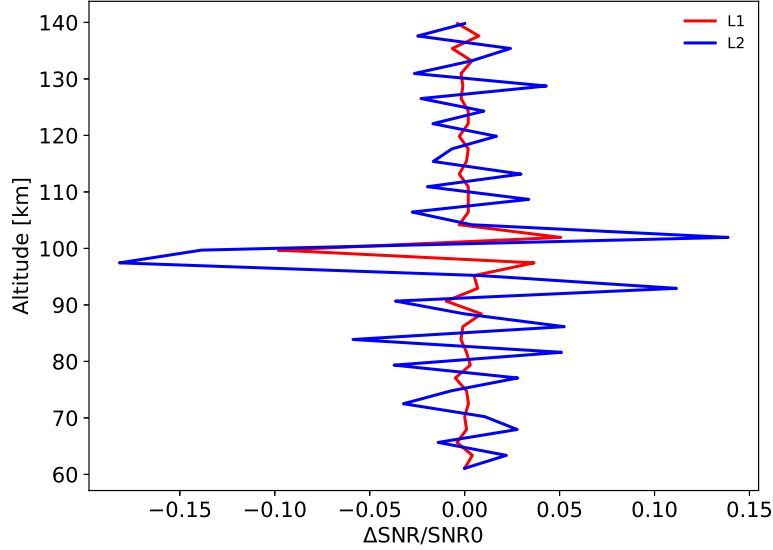
Figure 13. An example of the detrended SNR for both the L_1 and L_2 signals.

3.2.4 Yu et al. (2020) Method

From the 50 Hz COSMIC (atmPhs) L_1 SNR data, a 50 point window of (25 below and above) is used to calculate a 1 Hz S_4. This S_4 is calculated as a function of altitude and is converted to an foEs following:

$$(foEs - 1.2)^2 = 13.62 * S_{4,Max},$$ (10)

where the $S_{4,Max}$ is the maximum of the S_4 index and the foEs is the peak frequency of the sporadic-E cloud. Yu et al. (2020) developed a high resolution and high sensitivity RO technique to determine the global distribution of sporadic-E layer intensities at a high spatial and temporal resolution, including weak sporadic-E layers that are below thresholds of reliable detection for ground-based ionosondes. An example of the S_4 as a function of altitude is displayed in Figure 14.
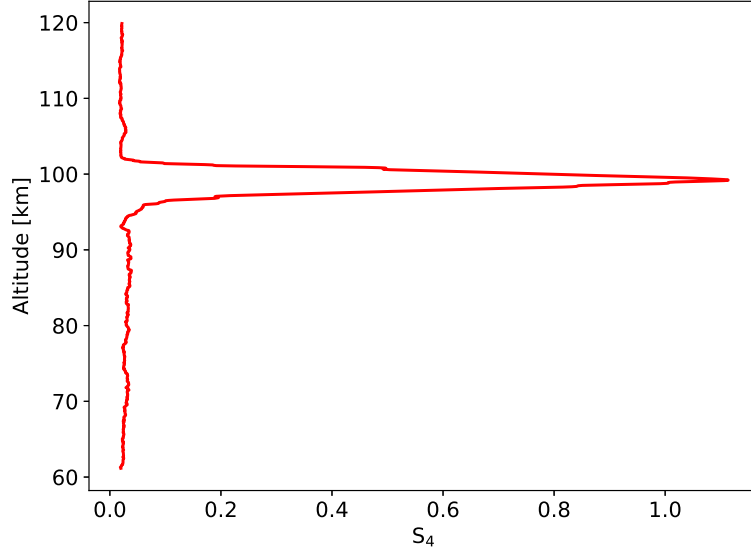
Figure 14. An example of L_1 S_4 as a function of altitude. The maximum S_4 values is used to estimate an fbEs.

3.2.5 Gooch et al. (2020) Method

Using the 50 Hz COSMIC (atmPhs) excess phase data, a $TEC_{Background}$ is calculated using Equation 1 and smoothed with a 1 km interval. From there, the $TEC_{Smoothed}$ is detrended using a Savitzky-Golay filter with a 25 km window as displayed in Figure 15. The electron density is calculated from

$$\Delta n_e = \frac{TEC_{Smoothed} - TEC_{Background}}{2\sqrt{2r\Delta r}}, \tag{11}$$

where the detrended TEC is divided by an effective path length of 176 km corresponding to an effective path through a cylinder with a vertical thickness of $\Delta r = 0.6$ km (Gooch et al., 2020). The effective path length is derived from an assumed geometry of a cylinder centered around the tangent point (Ahmad, 1999). Gooch et al. (2020)

provided insight into bias and limitations of three GPS-RO methods for estimating sporadic-E intensities for the years 2010 and 2014. .
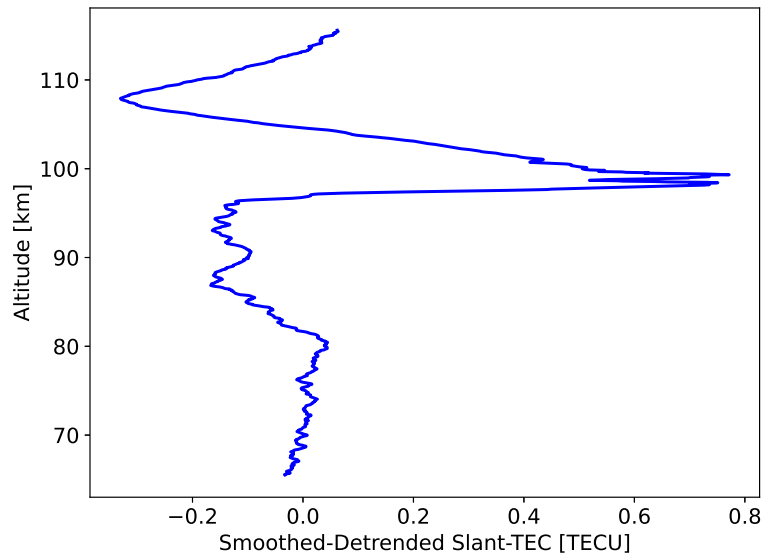
Figure 15. An example of 50 Hz detrended TEC used to calculate a sporadic-E electron density through division by an effective path length.

3.3 Ionosonde and GPS-RO Comparison

To compare RO and ionosonde occurrence rates, the number of RO tangent point crossings at an altitude of 100 km within 170 km of each Digisonde site are counted. This 170 km used for the spatial separation corresponds to the average length of sporadic-E (Cathey, 1969). A map of the 32 Digisonde sites and corresponding areas used to compare with RO are displayed in Figure 16. A threshold fbEs of 3 MHz is used to count the binary sporadic-E presence. Occurrence rates are calculated by dividing the total number of sporadic-E occurrences by the total number of measurements for some time period (seasonal or entire year).
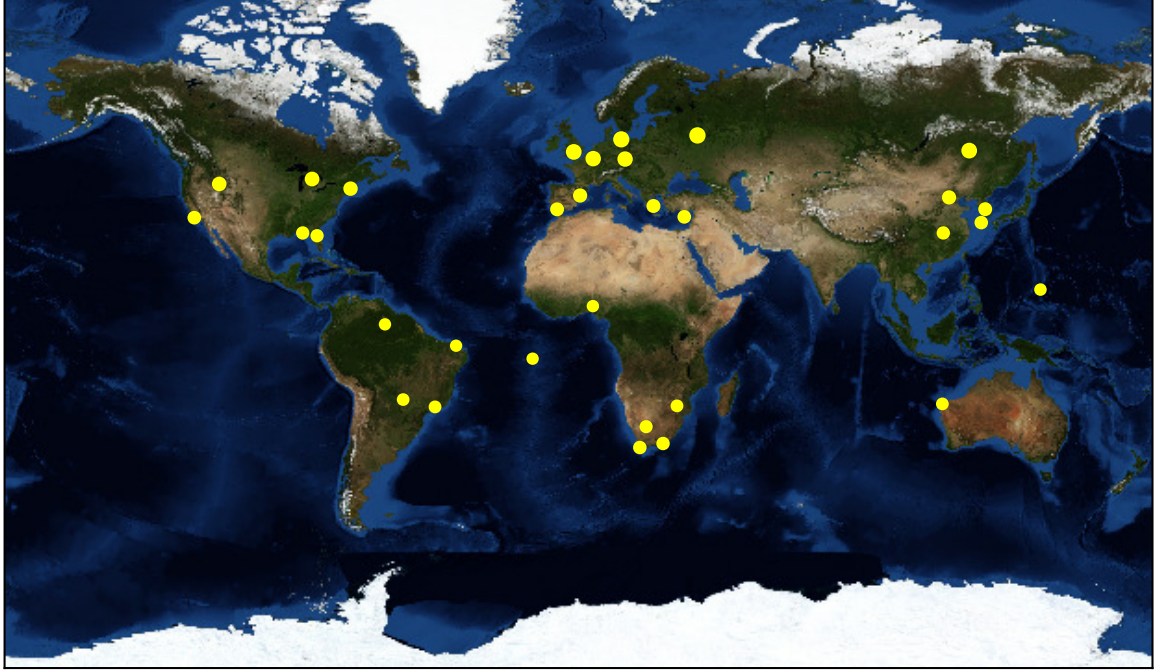
Figure 16. Map of the Digisonde sites and areas used for GPS-RO calculations corresponding to the range of 170 km shaded yellow.

Digisonde data that has been used for this project are restricted to data auto-scaled by ARTIST-5 to standardize the results. ARTIST-5 is the latest version of auto-scaling software and provides the most advanced methods for estimating sporadic-E parameters compared to older versions of ARTIST (results not shown). Additionally, the occurrence rates calculated for the Digisondes check to ensure there are at least 2 ionograms per hour over the course of a year.

An informative method to find the mean and median of the occurrence rates requires the use a bootstrapping approach with a sample size of 10,000 and confidence interval of 95% to analyze statistical similarity between the RO and ionosonde measurements. A bootstrapping approach is used to estimate a population of data by sampling a dataset replacement (Brownlee, 2019). Another method for comparison is to plot occurrence rates as a function of latitude to determine how each site performed with respect to location. This helps to see how occurrence rates change seasonally in

each hemisphere. With the latitude plots a rolling average trend line can be added with a 10 degree window. Using an ellipse plot for GPS-RO ratios against Digisonde ratios can show graphically the covariance to the second standard deviation. This provides a measure of the data spread in for both measurements of interest. Another comparison method is to compare linear fits of the ratios and compare against the expected one-to-one line. Using the same GPS-RO ratios against the Digisonde ratios error bars can be calculated per site to find accuracy of the data. A cumulative probability distribution of the errors in GPS-RO estimates provides a measure of the error spread for the different techniques. Separating the data into seasonal 3 month increments provides a more accurate comparison of results since each hemisphere of the Earth behaves differently depending on the time of year (Arras and Wickert, 2018; Chu et al., 2010).

IV. Results

This chapter presents a comparison between GPS-RO and ionosonde based occurrence rates of sporadic-E across the globe over the years 2010-2017. First, the summer and winter seasons are compared, followed by spring and fall, and finally all seasons combined. The seasonal comparisons are required because of the highly seasonal nature of sporadic-E, ensuring the occurrence rates from the different measurements are observed over the same season.

4.1 Winter and Summer Comparison

The figures that compare the GPS-RO ratio to the Digisonde ratio are displayed in Figure 17 for winter and Figure 18 for summer. Each GPS-RO technique is compared to the ionosonde results for each Digisonde site for the season over the years 2010-2017. The linear fit provides a measure of the general trend and should be compared against the expected one-to-one line. In the winter season, Gooch (green) and Niu (cyan) overestimate the occurrence rates. However, the slope of the two methods correlates to the Digisonde ratios as increases with value. The Arras (red) method overestimates the slope which will increase the over estimation rate as the actual (ionosonde) occurrence rate values increase. The Chu (blue) methodology underestimates both the occurrence rates and slope. The Yu (yellow) method has the closest occurrence rates but the slope is lower which would increase the gap between the Digisonde ratios for larger ionosonde occurrence rates. In the summer season Chu (blue) underestimates and Arras (red) and Gooch (green) overestimate the rates. Yu (yellow) and Niu (cyan) are near the one-to-one ratio (dashed black line) however their slopes are leass than one which will lead to underestimating if there were higher ratios.

Figure 17. Dec, Jan, and Feb 2010-2017: Sporadic-E occurrence rates for the GPS-RO methods and the Digisonde observations with a linear fit for each method.

Figure 18. Jun, Jul, and Aug 2010-2017: Sporadic-E occurrence rates for the GPS-RO methods and the Digisonde observations with a linear fit for each method.

Figure 19 and Figure 20 show the 95% confidence ellipses of each technique for winter and summer, respectively. They show the area where most of the values lie within the scatter plot and provide a visual representation of where the techniques stand relative to each other. In the summer and winter Arras (red), Niu (cyan), and Gooch (green) overestimate the rates and Chu (blue) underestimates. Yu (yellow) falls mostly centered with values both over and under estimating. The confidence ellipse thicknesses demonstrate a wide variability in the GPS-RO measurements for each technique.
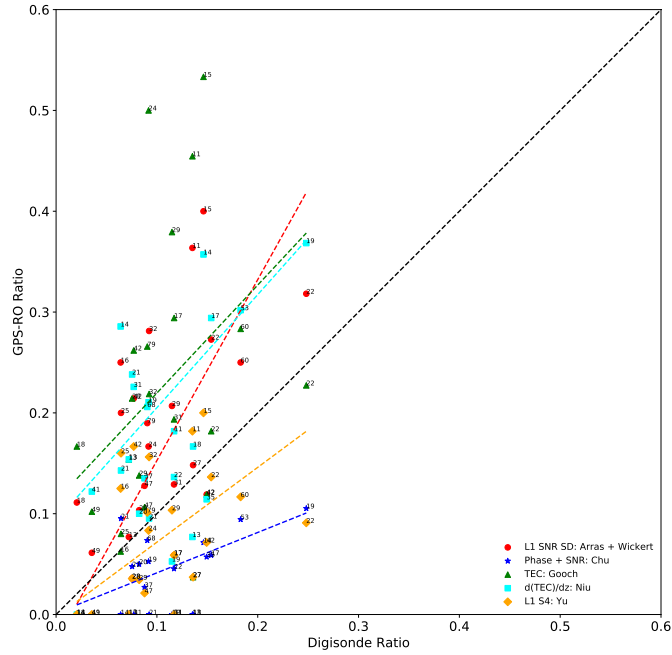

Figure 19. Dec, Jan, and Feb 2010-2017: Sporadic-E occurrence rates for the GPS-RO methods and the Digisonde observations with a confidence ellipse corresponding to two standard deviations (95%).
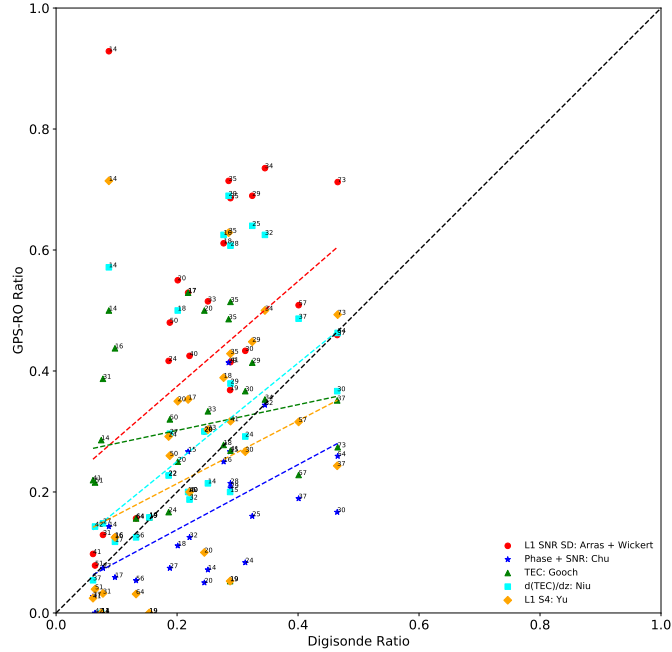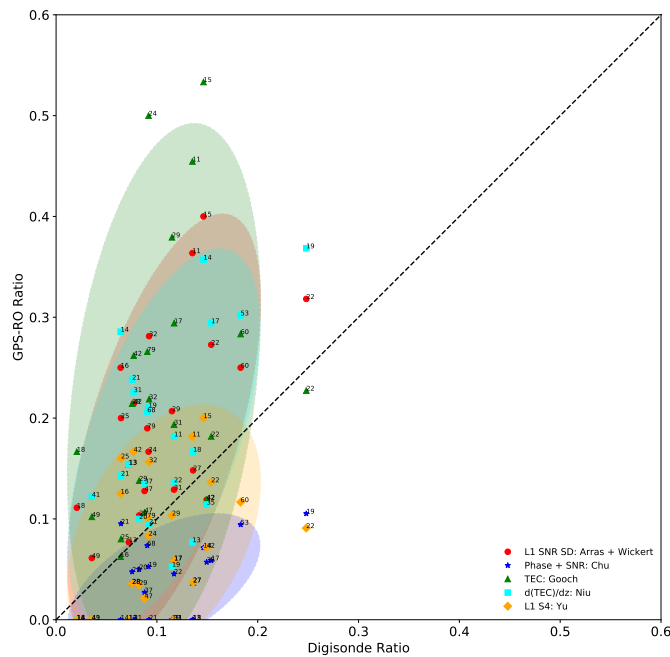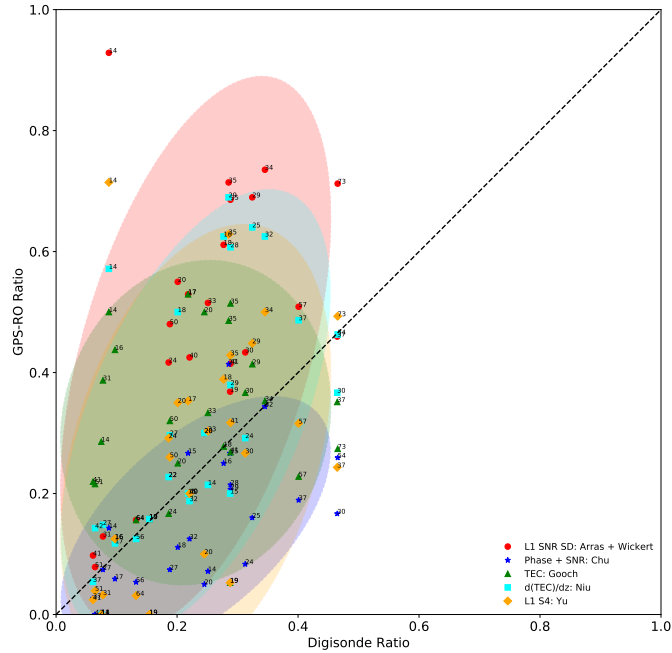
Figure 20. Jun, Jul, and Aug 2010-2017: Sporadic-E occurrence rates for the GPS-RO methods and the Digisonde observations with a confidence ellipse corresponding to two standard deviations (95%).

The individual site uncertainties are displayed in Figure 21 for winter, and Figure 22 for summer. The uncertainties are calculated from the standard deviation for each technique at each site treating each year in 2010-2017 as a separate point. In the winter season Gooch (green) and Niu (cyan) techniques had the upper bounds for the largest uncertainties while Chu (blue) and Yu (yellow) had the smallest yearly fluctuations. In the summer season Arras (red) had the upper bounds and Chu (blue) had the lower. These error bars show how far each technique can vary from year-to-year and site-to-site.
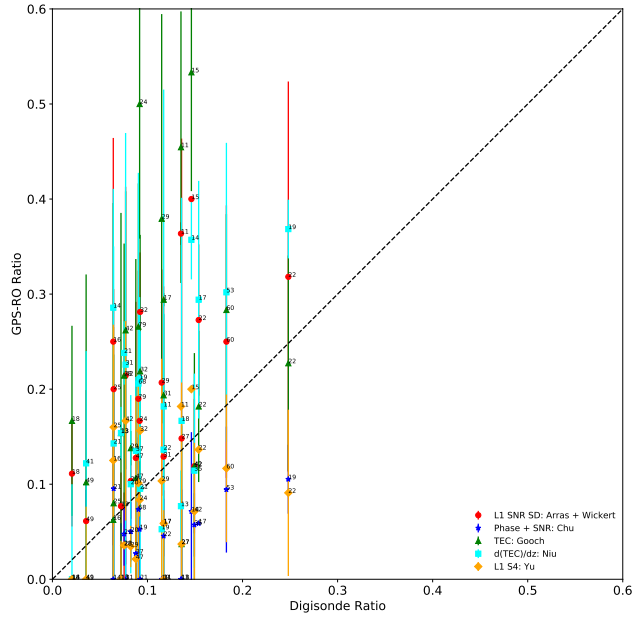
Figure 21. Dec, Jan, and Feb 2010-2017: Sporadic-E occurrence rates for the GPS-RO methods and the Digisonde observations showing the individual site uncertainty per method.
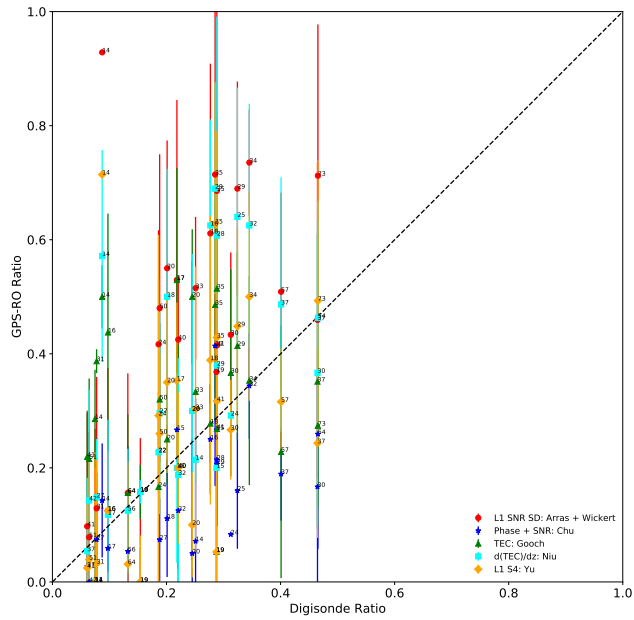
Figure 22. Jun, Jul, and Aug 2010-2017: Sporadic-E occurrence rates for the GPS-RO methods and the Digisonde observations showing the individual site uncertainty per method.

The occurrence rates as a function of latitude are displayed Figure 23 and Figure 24 for winter and summer, respectively. The expected latitude dependence of sporadic-E formation is immediately obvious, with a maximum in the local summer hemisphere. In the winter, all trendlines correlate with higher values in the lower latitude and lower values in the higher latitude. Arras (red), Niu (cyan), and Gooch (green) overestimate rates while Yu (yellow) and Chu (blue) underestimate. Yu is the closest to the actual value of the Digisonde data (dashed black line) and within the yearly uncertainty for the ionosonde data. In the summer season all but Chu overestimate the rates. However, Chu has the closest values and is within the uncertainty for multiple sites.
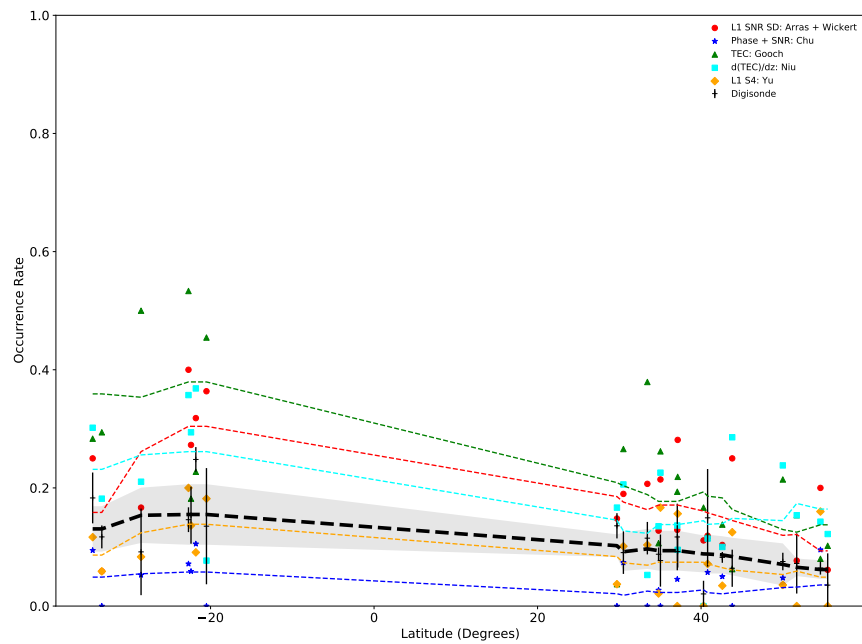
Figure 23. Dec, Jan, and Feb 2010-2017: Occurrence rates as a function of latitude with a rolling average of $\pm 10°$ for trendlines and shading for the Digisonde uncertainty.
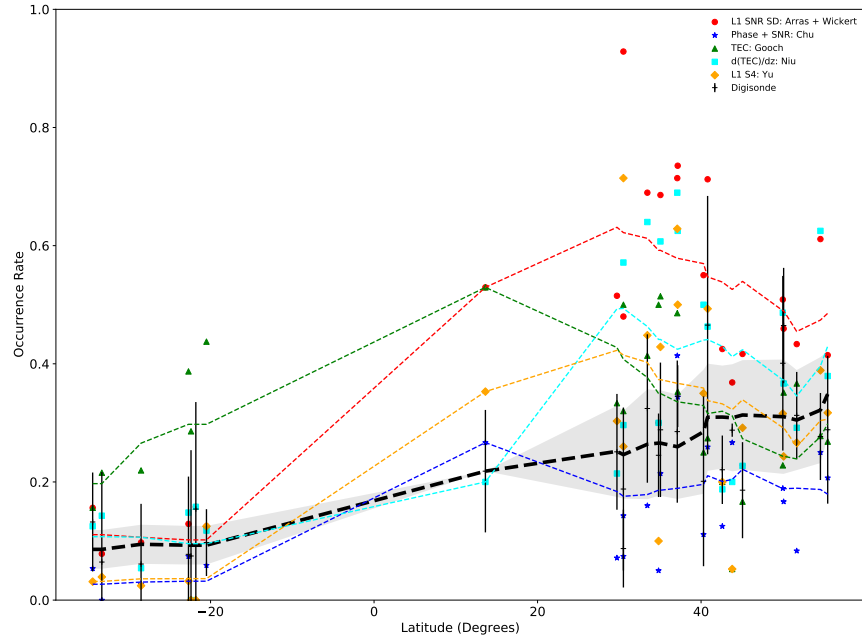
Figure 24. Jun, Jul, and Aug 2010-2017: Occurrence rates as a function of latitude with a rolling average of $\pm 10°$ for trendlines and shading for the Digisonde uncertainty.

The bootstrap calculated means using 10,000 random resamples are displayed in Figure 25 for winter and Figure 26 for summer. These figures show the mean and associated 95% confidence interval for each technique, providing a measure of statistical similarity between the measurement methods. The winter shows Arras (red), Gooch(green), and Niu (cyan) overestimating rates and not intersecting the confidence interval of the Digisonde data (shaded region). In the summer, Arras overestimates rates with Gooch and Niu but crosses the Digisonde confidence interval. Gooch and Niu crossed the Digisonde mean value (dotted black line) within the uncertainty for each technique. Chu (blue) underestimates rates and the Yu (yellow) mean value and confidence interval overlapped with the Digisonde data.

Figure 25. Dec, Jan, and Feb 2010-2017: Bootstrap calculated means and 95% confidence intervals for each GPS-RO technique compared to the ionosonde rates.
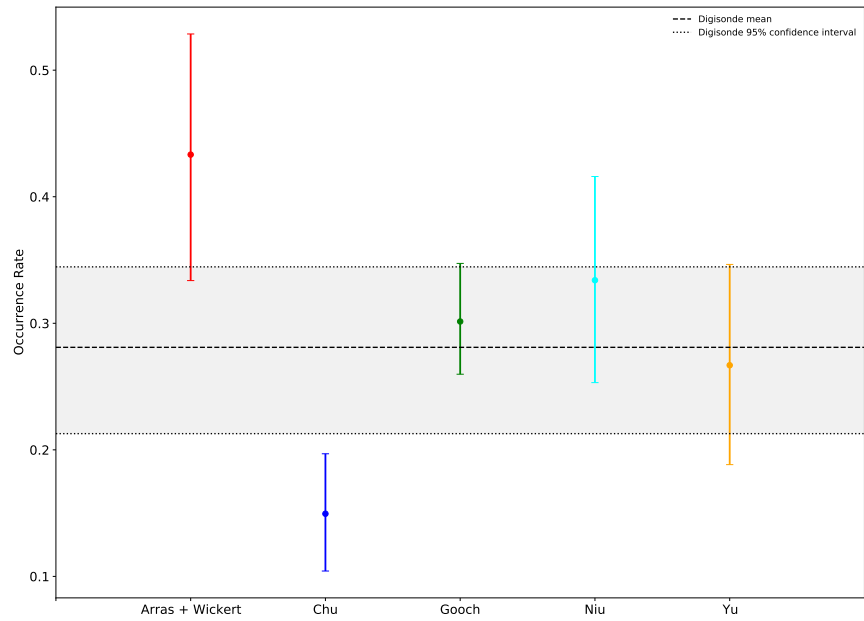
Figure 26. Jun, Jul, and Aug: 2010-2017: Bootstrap calculated means and 95% confidence intervals for each GPS-RO technique compared to the ionosonde rates.

The bootstrap calculated medians are displayed in Figure 27 for winter and Figure 28 for summer. The medians determine where the 50% point of the set is located. In the winter, only Yu (yellow) falls within the confidence interval (shaded region) of the Digisonde values. Chu (blue) underestimates and Arras (red), Gooch (green), and Niu (cyan) overestimate. In the summer season the confidence intervals overlap for Chu, Gooch, Niu, and Yu.
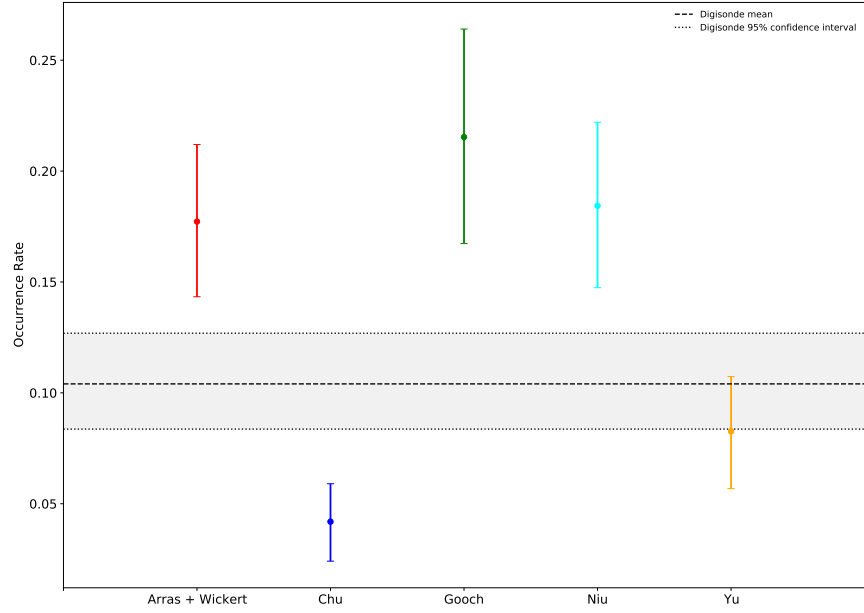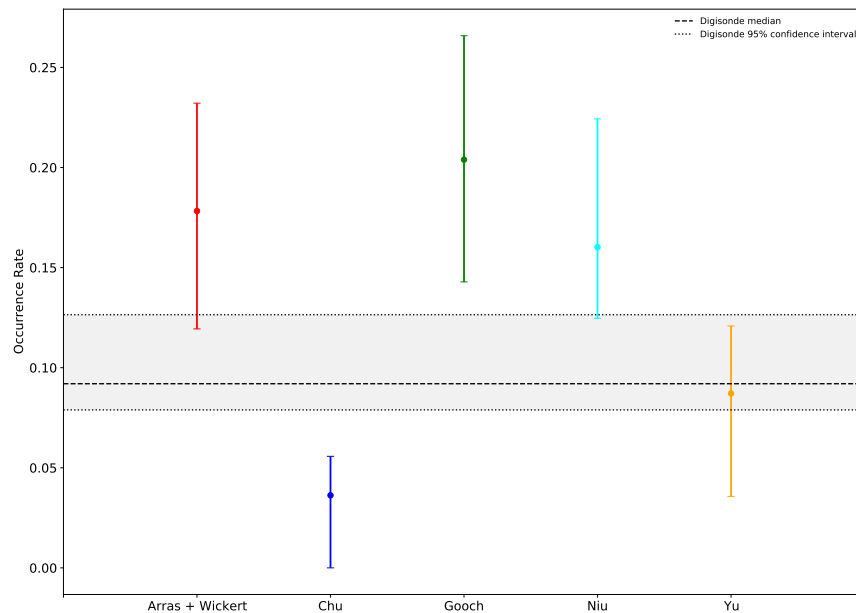

Figure 27. Dec, Jan, and Feb 2010-2017: Bootstrap calculated medians and 95% confidence intervals for each GPS-RO technique compared to the ionosonde rates.
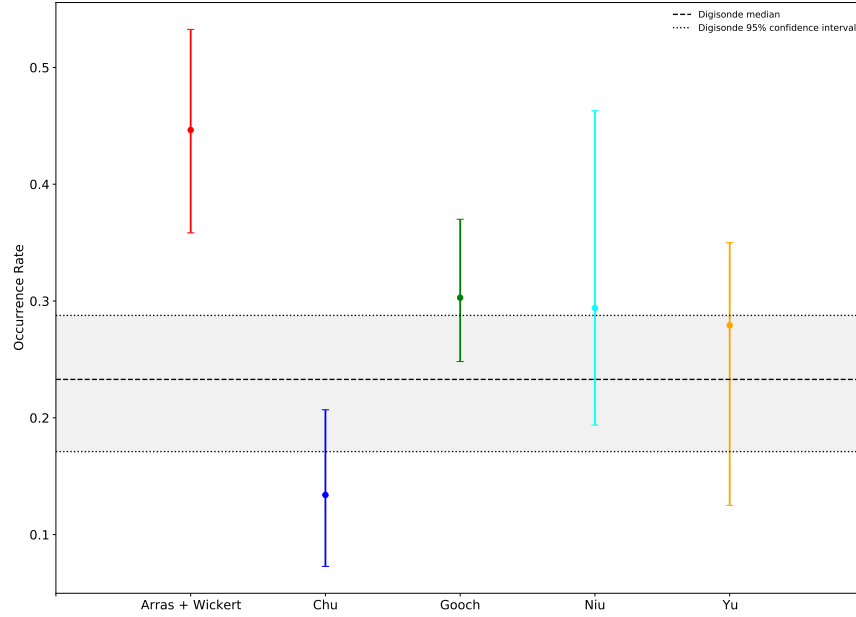
Figure 28. Jun, Jul, and Aug 2010-2017: Bootstrap calculated medians and 95% confidence intervals for each GPS-RO technique compared to the ionosonde rates.

The cumulative probability distributions for the ratio differences between the GPS-RO techniques and the ionosonde measurements are displayed in Figure 29 for winter and Figure 30 for summer. Each figure shows where the second standard deviation and first deviation lies (dotted black lines). In the winter, the Yu (yellow) cumulative probability arrives at the 68% and 95% values before the other methods. However, in the Summer Niu (cyan) reaches 68% first while Chu (blue) reaches the 95% first.
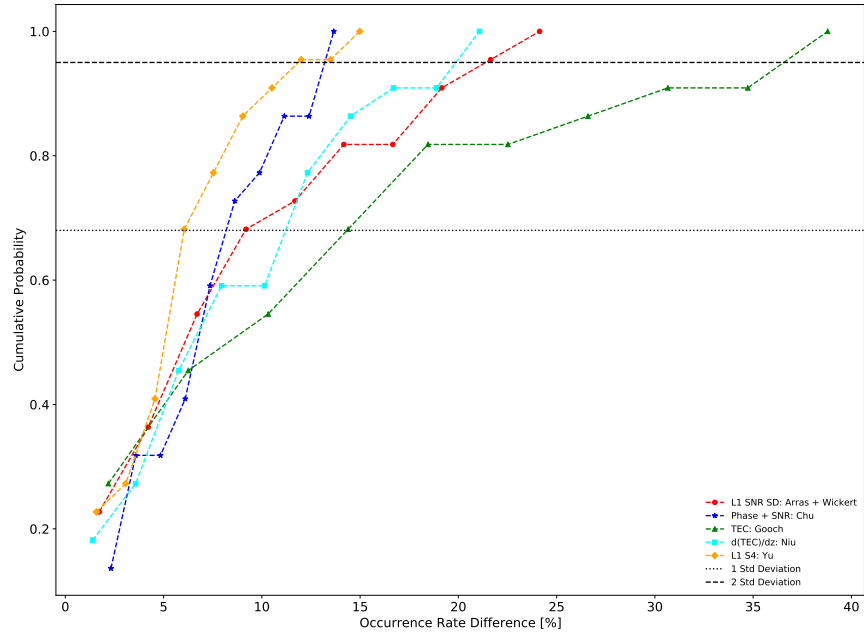
Figure 29. Dec, Jan, and Feb 2010-2017: Cumulative probability distributions for the occurrence rate differences between each GPS-RO technique and the ionosonde measurements.
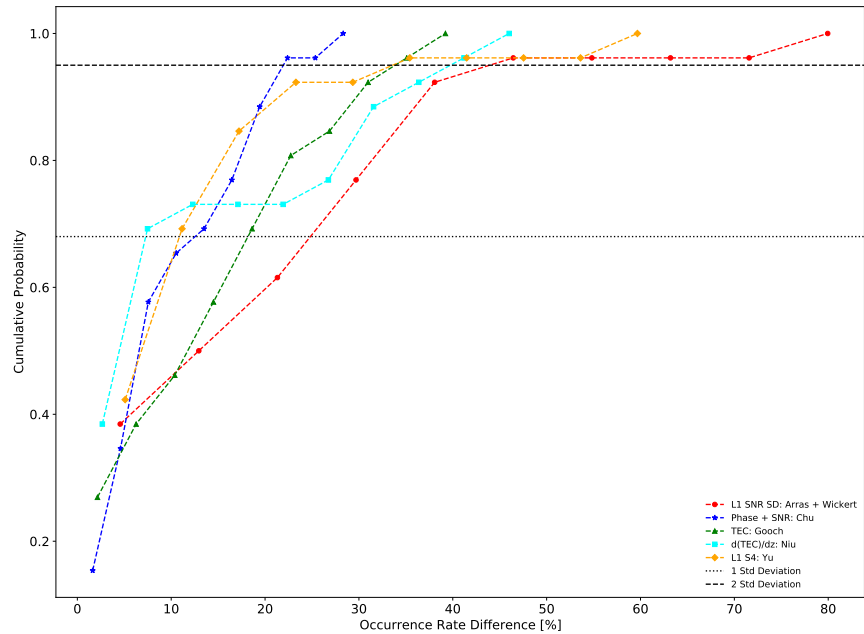
Figure 30. Jun, Jul, and Aug 2010-2017: Cumulative probability distributions for the occurrence rate differences between each GPS-RO technique and the ionosonde measurements.

4.2 Spring and Fall Comparison

In this section, the spring and fall seasons are analyzed to highlight differences and similarities in sporadic-E measurements outside of the maximum and minimum occurrences rates observed for summer and winter. Scatter plots of the occurrence rates with linear fits for the different GPS-RO techniques are displayed in Figure 31 for spring and Figure 32 for fall. The 95% confidence ellipses are shown in Figure 33 for spring and Figure 34 for fall. Individual site uncertainties and occurrence rates as a function of latitude are displayed in Figure 35 and Figure 37 for spring, and Figure 36 and Figure 38 for fall. The bootstrapped means and medians are shown in Figure 39 and Figure 41 for spring and Figure 40 and Figure 42 for fall. The cumulative probability distributions are displayed in Figure 43 for spring and Figure 44 for fall.

Figure 31. Mar, Apr, and May 2010-2017: Sporadic-E occurrence rates for the GPS-RO methods and the Digisonde observations with a linear fit for each method.
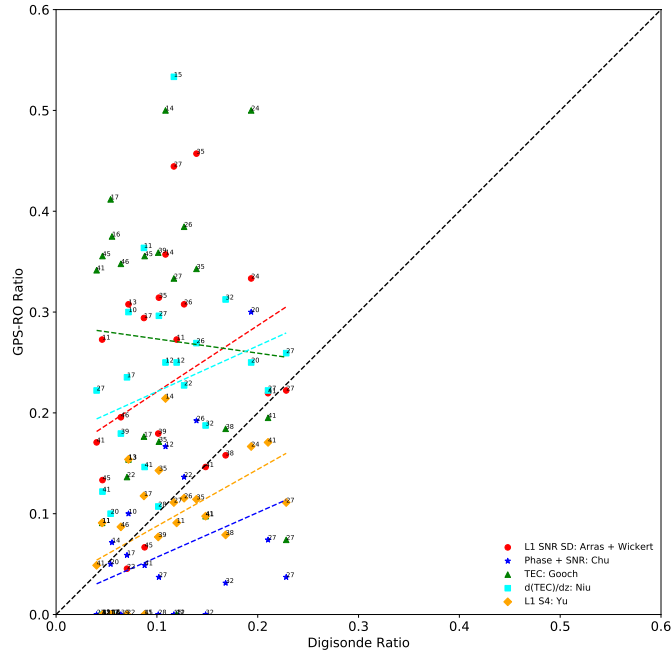
Figure 32. Sept, Oct, and Nov 2010-2017: Sporadic-E occurrence rates for the GPS-RO methods and the Digisonde observations with a linear fit for each method.

Overall, the results are similar to the summer and winter comparisons. Some notable differences included a negative slope for the Gooch technique in Figure 32, indicating a large overestimation of the low occurrence rates. The confidence ellipse of Figure 34 show a similar result with a nearly vertical ellipse for Gooch.

36
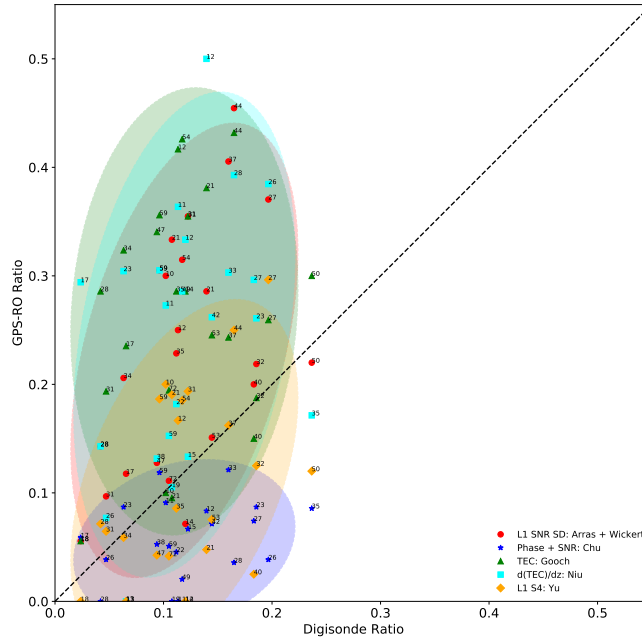
Figure 33. Mar, Apr, and May 2010-2017: Sporadic-E occurrence rates for the GPS-RO methods and the Digisonde observations with a confidence ellipse corresponding to two standard deviations (95%).
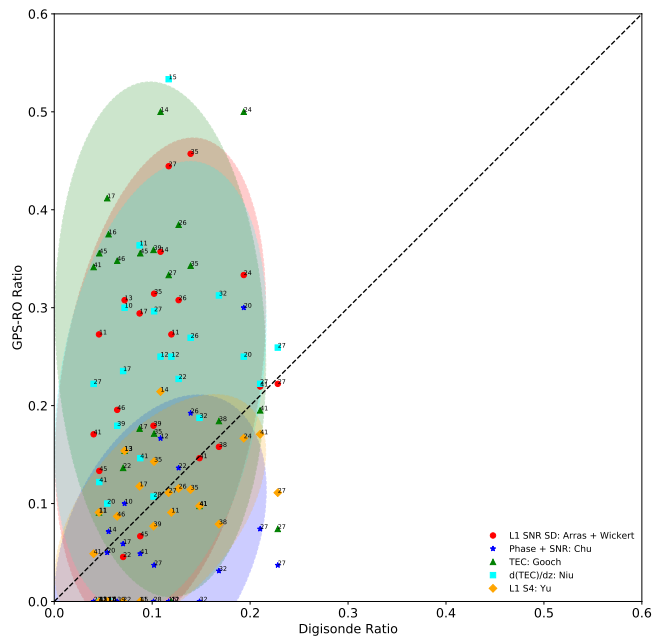
Figure 34. Sept, Oct, and Nov 2010-2017: Sporadic-E occurrence rates for the GPS-RO methods and the Digisonde observations with a confidence ellipse corresponding to two standard deviations (95%).
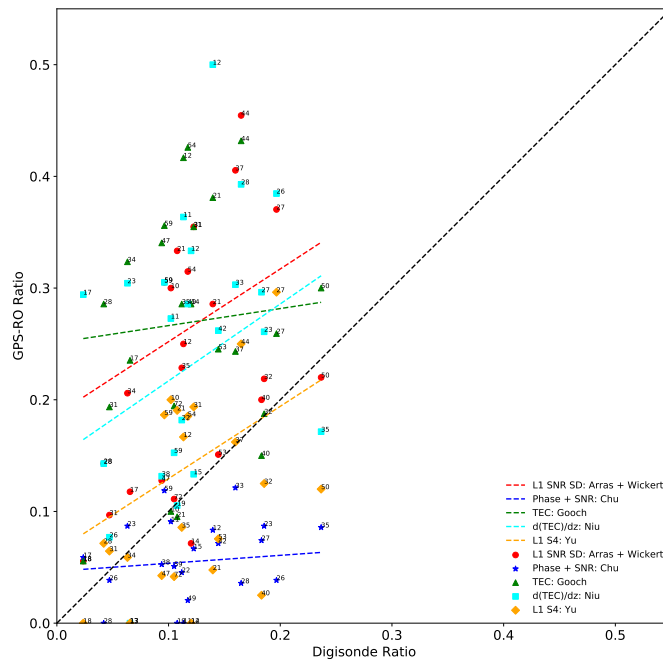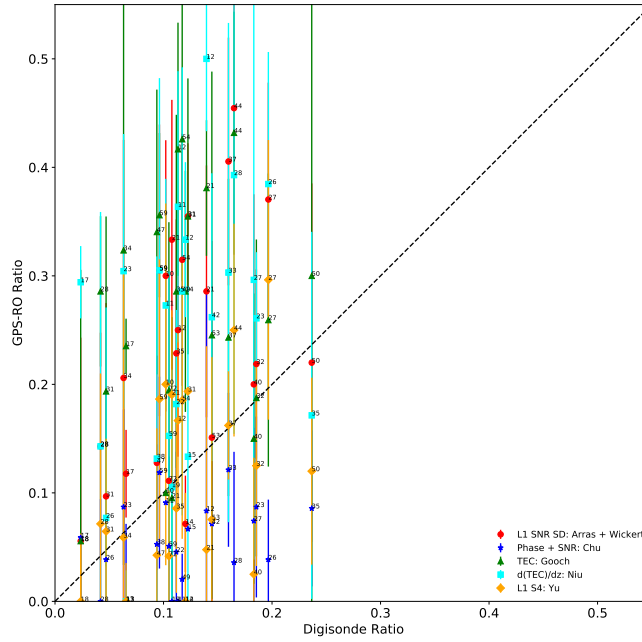
Figure 35. Mar, Apr, and May 2010-2017: Sporadic-E occurrence rates for the GPS-RO methods and the Digisonde observations showing the individual site uncertainty per method.
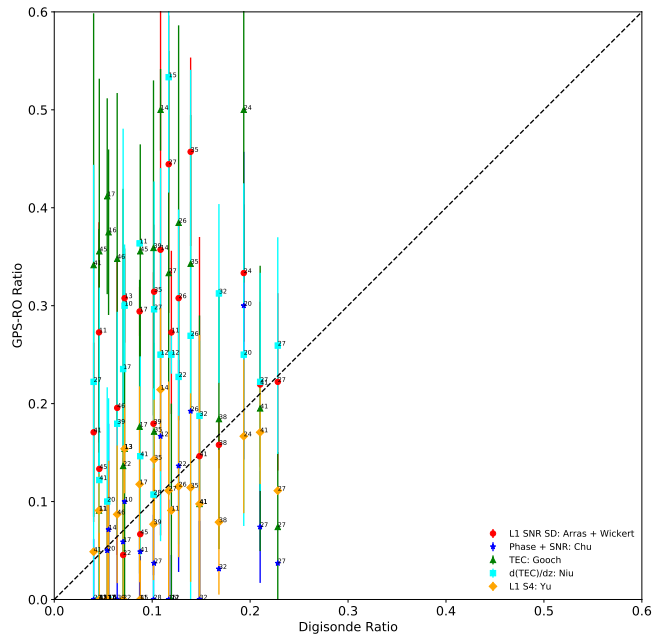
Figure 36. Sept, Oct, and Nov 2010-2017: Sporadic-E occurrence rates for the GPS-RO methods and the Digisonde observations showing the individual site uncertainty per method.

The Chu estimates no sporadic-E occurrence for $-20°$ to $0°$ latitude in May, Apr, and May (Figure 37). In this same latitude range, the ionosonde value is around 10%. For Sept, Oct, and Nov, the Chu technique falls within the ionosonde uncertainties for most latitudes (Figure 38). Similar to the summer and winter comparison, the Yu technique results align with the Digisonde results for most latitudes.
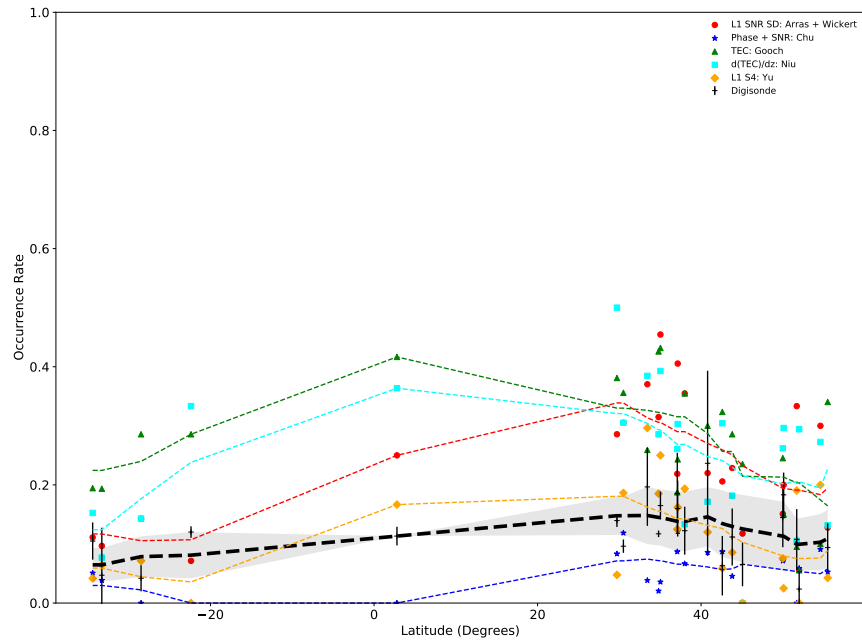
Figure 37. Mar, Apr, and May 2010-2017: Occurrence rates as a function of latitude with a rolling average of $\pm 10°$ for trendlines and shading for the Digisonde uncertainty.
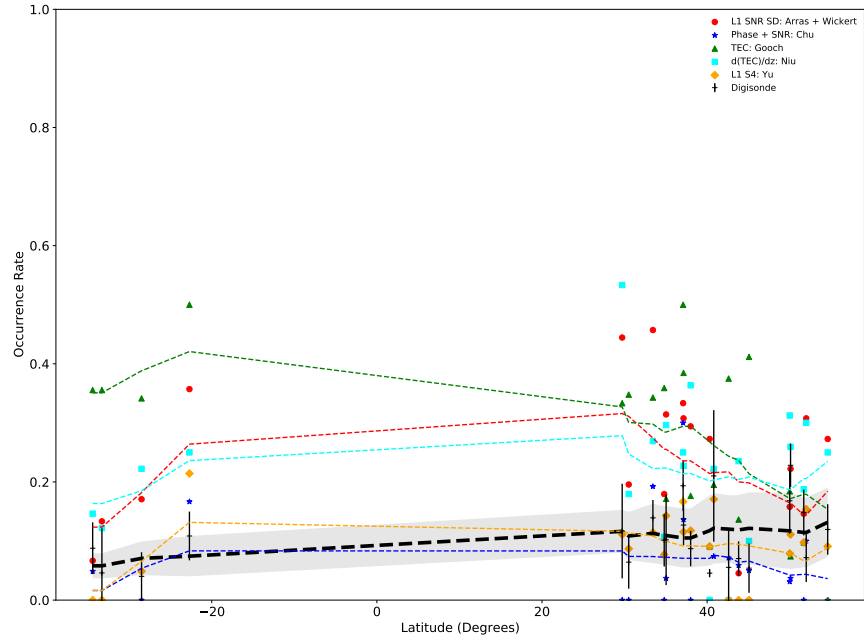
Figure 38. Sept, Oct, and Nov 2010-2017: Occurrence rates as a function of latitude with a rolling average of $\pm 10°$ for trendlines and shading for the Digisonde uncertainty.

For the fall and spring bootstrapped means and medians, the Yu technique is the only technique to fall within the ionosonde confidence interval. Chu underestimates the rates while Niu, Gooch, and Arras overestimate.
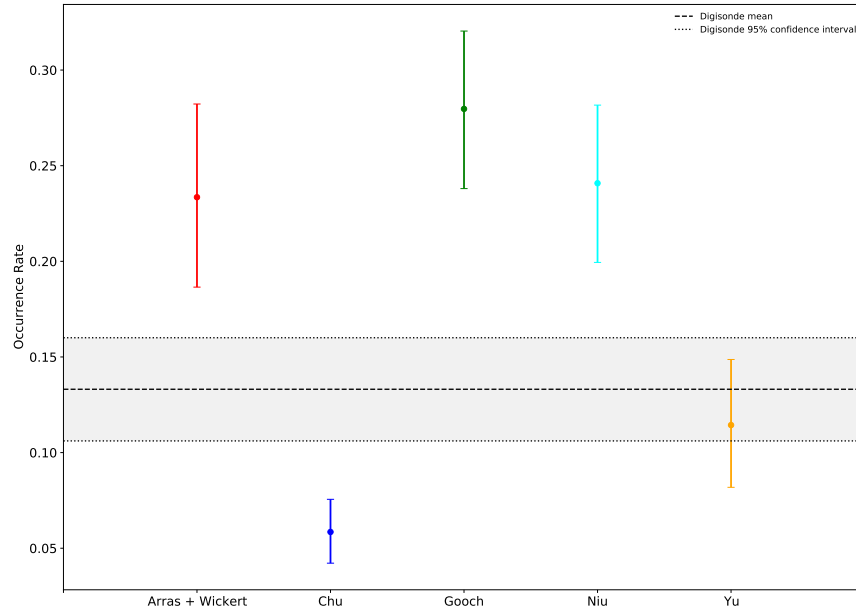
Figure 39. Mar, Apr, and May 2010-2017: Bootstrap calculated means and 95% confidence intervals for each GPS-RO technique compared to the ionosonde rates.
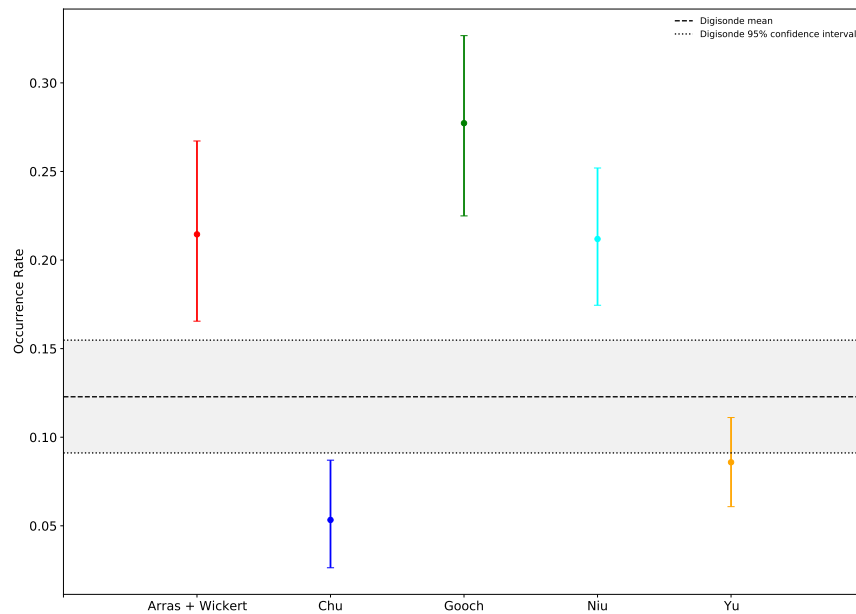
Figure 40. Sept, Oct, and Nov 2010-2017: Bootstrap calculated means and 95% confidence intervals for each GPS-RO technique compared to the ionosonde rates.
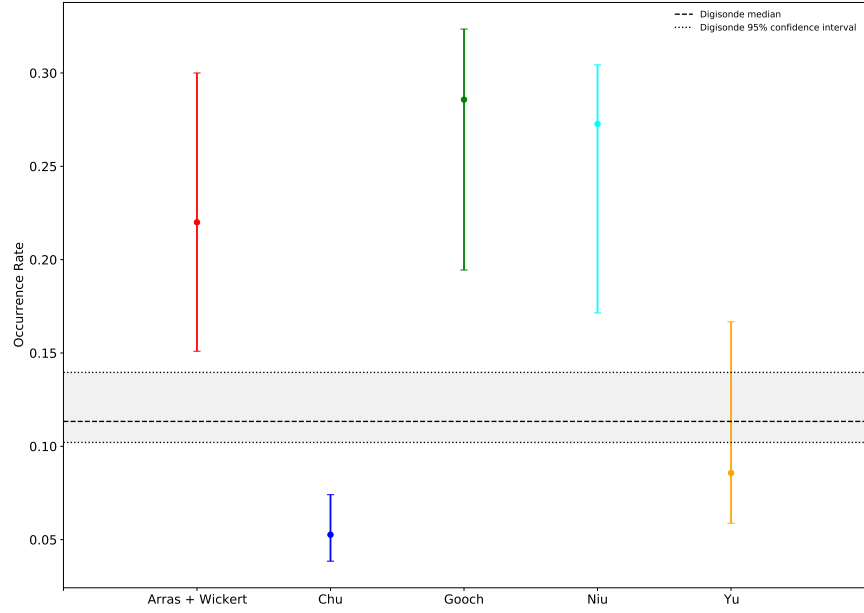
Figure 41. Mar, Apr, and May 2010-2017: Bootstrap calculated medians and 95% confidence intervals for each GPS-RO technique compared to the ionosonde rates.

Figure 42. Sept, Oct, and Nov 2010-2017: Bootstrap calculated medians and 95% confidence intervals for each GPS-RO technique compared to the ionosonde rates.

Figure 43. Mar, Apr, and May 2010-2017: Cumulative probability distributions for the occurrence rate differences between each GPS-RO technique and the ionosonde measurements.
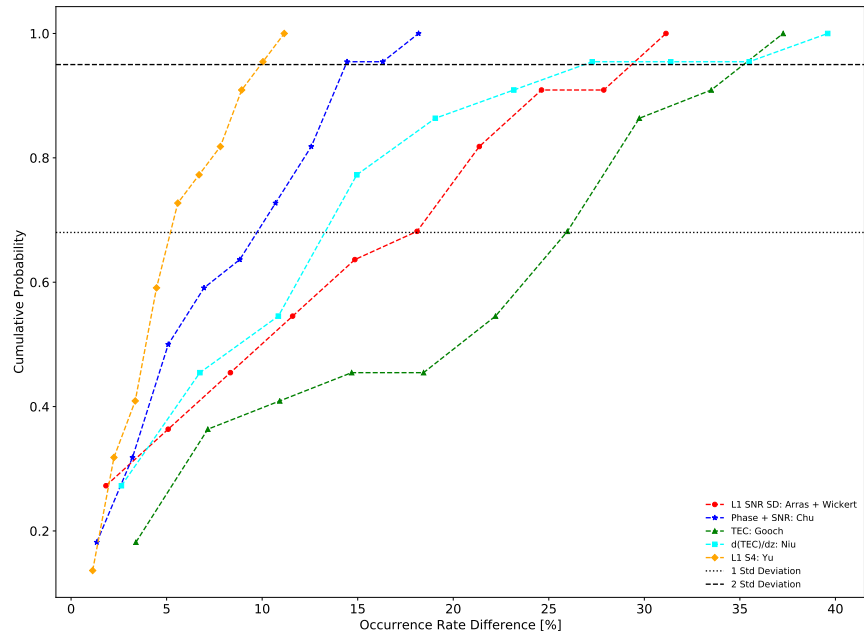
Figure 44. Sept, Oct, and Nov 2010-2017: Cumulative probability distributions for the occurrence rate differences between each GPS-RO technique and the ionosonde measurements.

4.3 Whole Year Comparison

In this section, the whole year (all seasons) are compared with no separation by
season. While these results are helpful for analyzing the entire datasets, care must be
taken with the interpretation of results due to the highly seasonal nature of sporadic-
E. Some measurements may not be uniformly distributed throughout the year, which
would induce a seasonal weighting to the data.

The scatter plot and linear fits of the GPS-RO to ionosonde ratios are displayed in
Figure 45. Both the Yu and Gooch slopes are negative, and the Chu, Arras, and Niu
slopes are much less than one. However, the Yu trend crosses the one-to-one line while
the other techniques are primarily above or below this line. Confidence ellipses are
displayed in Figure 46, which show nearly vertical ellipses for all techniques outside of
Chu. Uncertainties for the different sites and techniques are displayed in Figure 47.
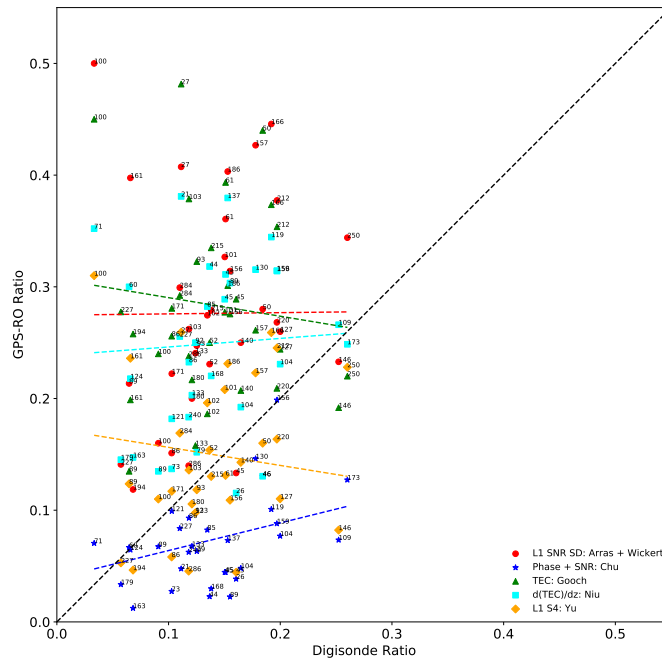
**Figure 45. 2010-2017: Sporadic-E occurrence rates for the GPS-RO methods and the
Digisonde observations with a linear fit for each method.**
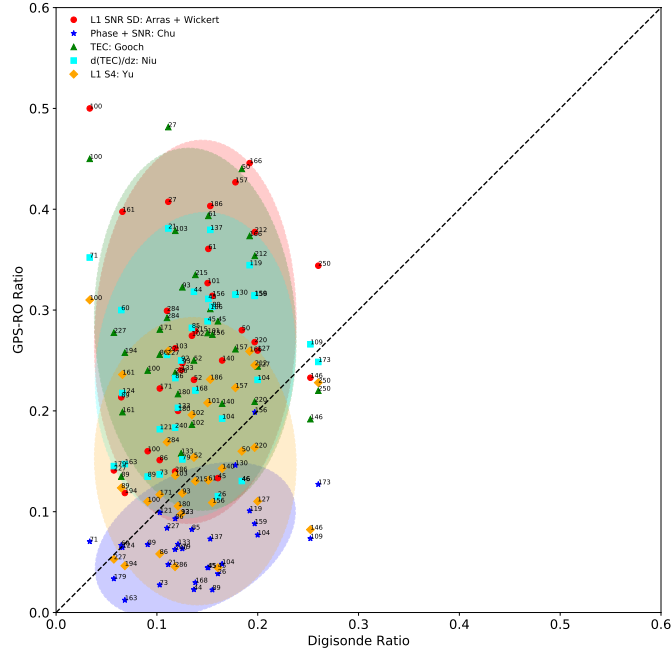
Figure 46. **2010-2017: Sporadic-E occurrence rates for the GPS-RO methods and the Digisonde observations with a confidence ellipse corresponding to two standard deviations (95%).**
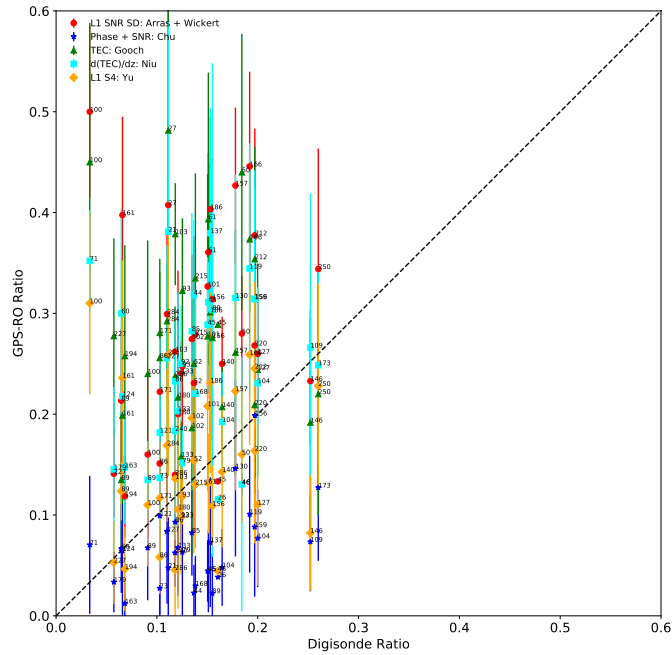
Figure 47. 2010-2017: Sporadic-E occurrence rates for the GPS-RO methods and the Digisonde observations showing the individual site uncertainty per method.

The latitude dependence of the sporadic-E rates averaged over the entire year shows fbEs occurrence rates around 10% with a slight increase in rates for the northern hemisphere (Figure 48). Similar to the seasonal results, the Chu technique tends to underestimate the rates, while Gooch, Arras, and Niu tend to overestimate. The Yu technique is within the ionosonde uncertainty for most latitudes.
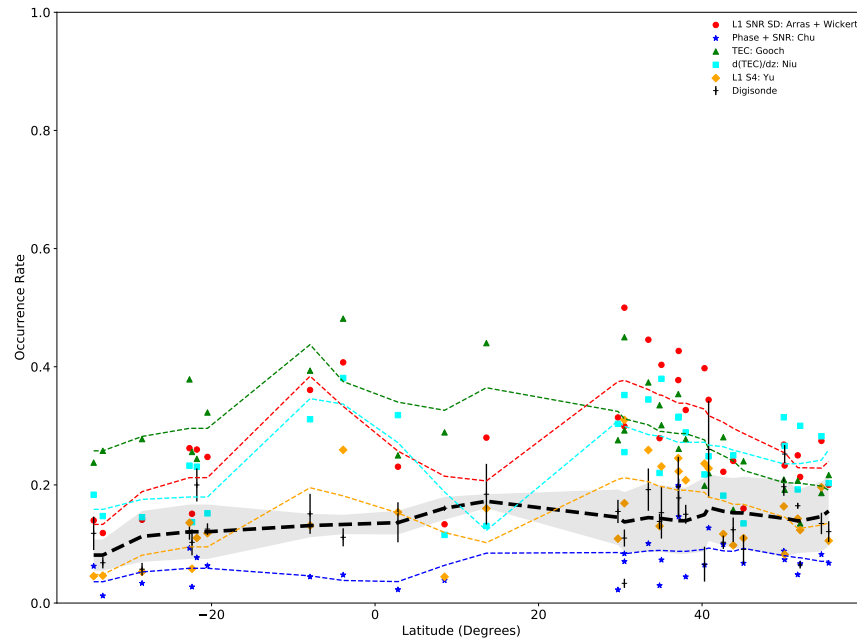
Figure 48. 2010-2017: Occurrence rates as a function of latitude with a rolling average of $\pm 10°$ for trendlines and shading for the Digisonde uncertainty.

The most valuable comparisons over all seasons are the mean (Figure 49) and median (Figure 50) which show whether or not the GPS-RO techniques are within the correct range of magnitudes overall. Both the mean and median show that the Yu technique provides the correct occurrence rate magnitude nearly matching the ionosonde results. The Niu, Arras, and Gooch techniques overestimate the rates while Chu underestimates.

46
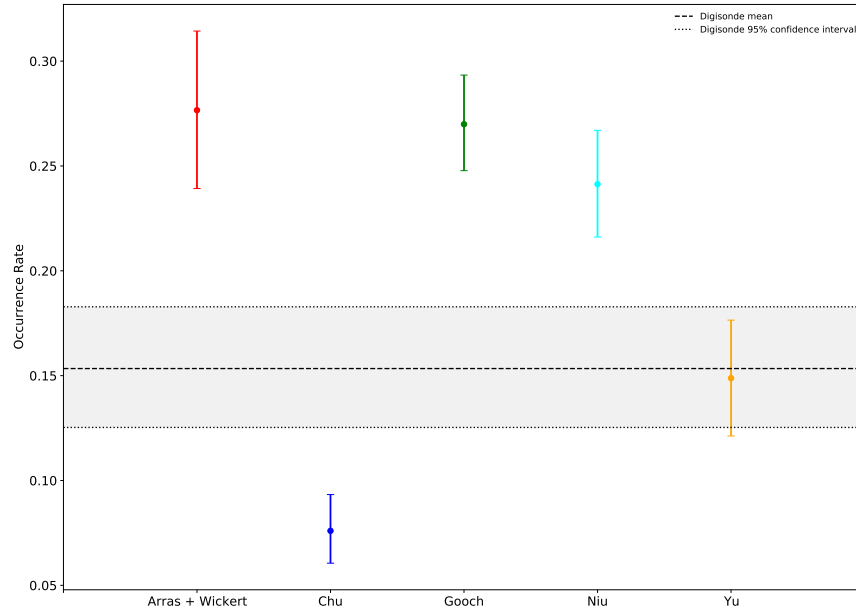
Figure 49. 2010-2017: Bootstrap calculated means and 95% confidence intervals for each GPS-RO technique compared to the ionosonde rates.
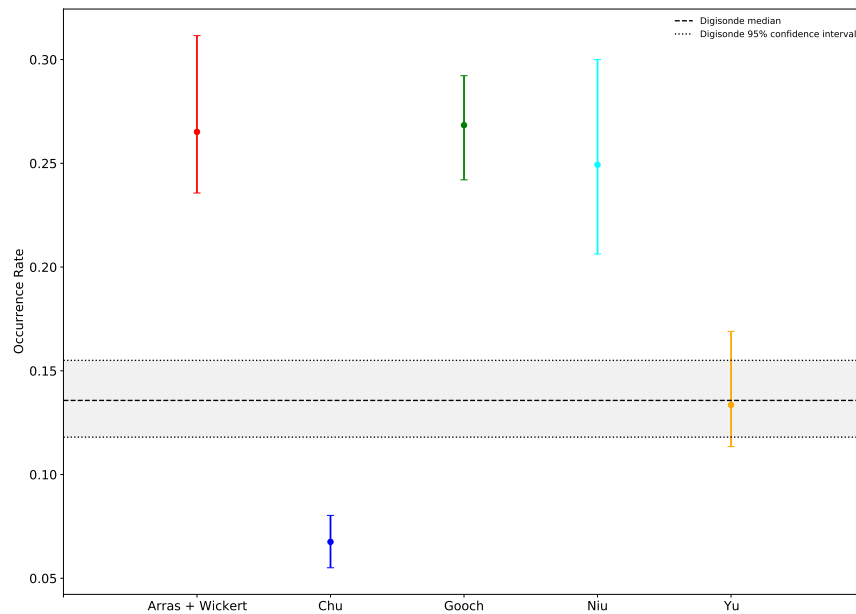
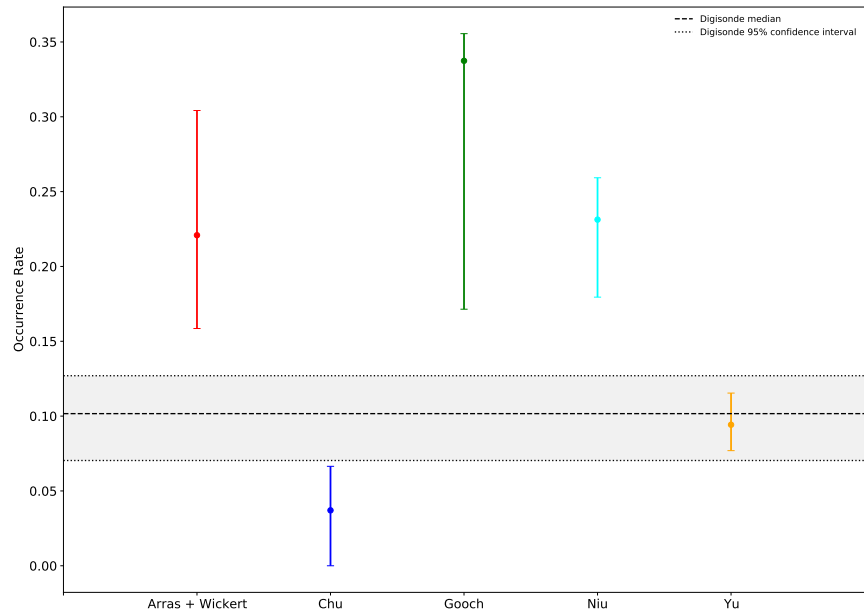

Figure 50. 2010-2017: Bootstrap calculated medians and 95% confidence intervals for each GPS-RO technique compared to the ionosonde rates.

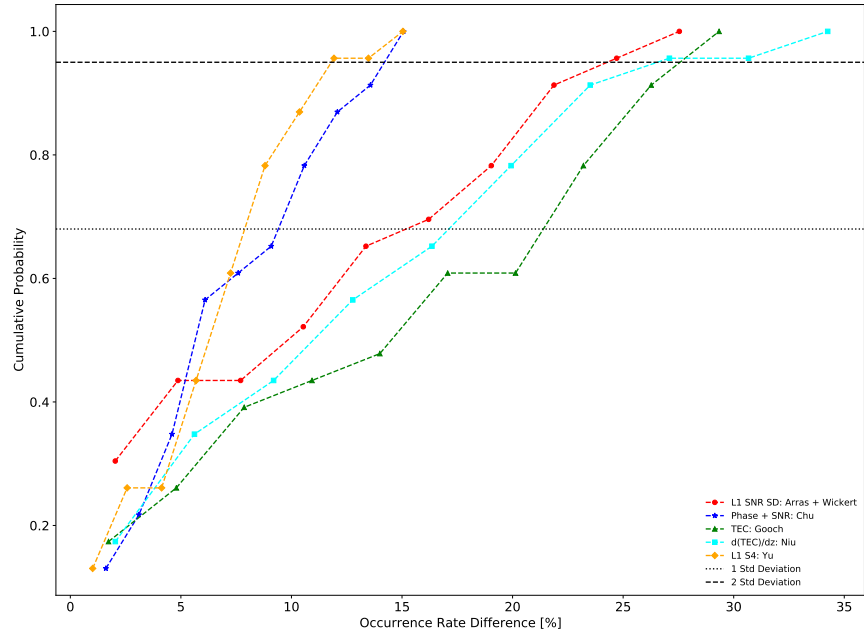The cumulative probability distributions (Figure 51) indicate the the Yu technique

minimizes error for 68% of the data, but the Chu technique minimizes the error if this is extended to 95%. While the Chu technique tends to underestimate the rates overall, the magnitude of the differences are smaller than the differences for the techniques that overestime the occurrence rates.
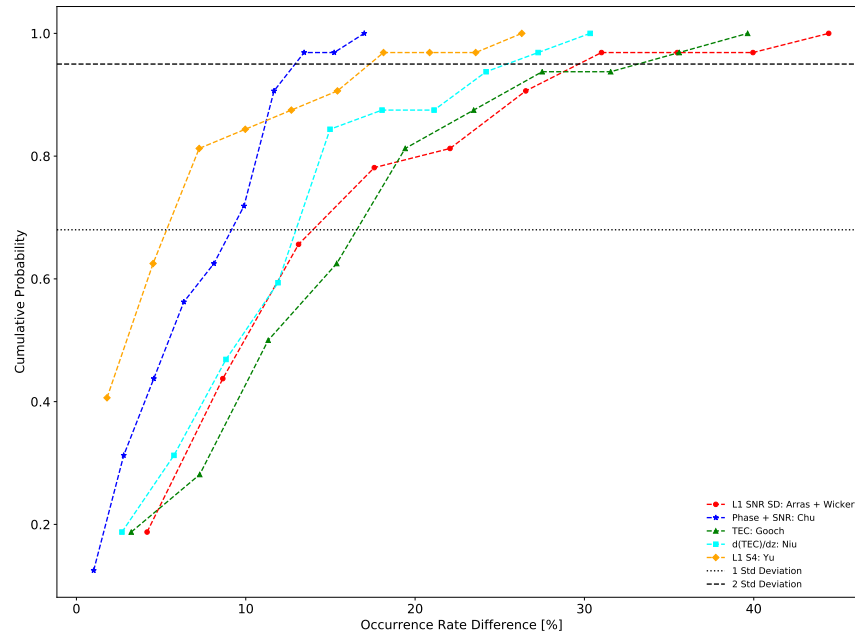
Figure 51. 2010-2017: Cumulative probability distributions for the occurrence rate differences between each GPS-RO technique and the ionosonde measurements..

4.4 Statistical Analysis

To compare the methods statistically we must combine the weighting for each method and the Digisonde weight. Here, the data is weighted by the total number of measurements. Afterward, the mean absolute error can be computed along with the relative error. We can also compute the average, standard deviation, correlation, and the statistical similarity of each method against the Digisonde numbers. Table 2 shows the average ratio over eight years for each technique along with the number of Digisonde observations and radio occultations averaged over all sites. The overall ratio from ionosonde observations (0.15) is closely matched by Yu while Chu underestimates

48

and Arras, Gooch, and Niu overestimate.

Table 2. Digisonde and GPS-RO ratios and the number of observations averaged over all sites.

Technique	Total RO	Total E_s	Ratio
Digisonde	209,040	32,313	0.15
Arras	144	40	0.28
Gooch	144	39	0.28
Yu	144	21	0.15
Chu	109	8	0.07
Niu	109	26	0.25

Table 3 shows the sporadic-E occurrence rate averages and standard deviations. Observed averages of ionosonde occurrence rates is between 0.10 and 0.28 for the four seasons and as a whole 0.16. Arras, Gooch, and Niu methods overestimated these rates from 0.18 to 0.43. The Chu method underestimated with 0.04 through 0.15. The Yu methodology was more inline with rates at 0.08 through 0.27. The ionosonde standard deviation for the whole year was 0.06 and was closely aligned with Gooch, Niu, and Yu at 0.07. Chu underestimated the standard deviation with 0.04 and Arras was over with 0.10.

Table 3. Digisonde and GPS-RO occurrence rate averages and standard deviations.

Technique	Dec-Feb	Mar-May	Jun-Aug	Sept-Nov	Whole Year
Digisonde Avg	0.10	0.13	0.28	0.12	0.16
Digisonde Std	0.05	0.06	0.13	0.06	0.06
Arras Avg	0.18	0.23	0.43	0.21	0.28
Arras Std	0.08	0.11	0.23	0.12	0.10
Chu Avg	0.04	0.06	0.15	0.05	0.08
Chu Std	0.04	0.04	0.11	0.07	0.04
Gooch Avg	0.22	0.28	0.30	0.28	0.27
Gooch Std	0.12	0.10	0.11	0.12	0.07
Niu Avg	0.19	0.24	0.33	0.21	0.24
Niu Std	0.09	0.10	0.20	0.10	0.07
Yu Avg	0.08	0.11	0.27	0.09	0.15
Yu Std	0.06	0.08	0.19	0.06	0.07

Table 4 shows the mean absolute error (MAE) which is the statistical measurement of the model performance error (Botchkarev, 2018; Willmott and Matsuura, 2005). This MAE is calculated in relation to the ionosonde observations. The lowest throughout most of the year was the Yu method ranging from 0.05 to 0.10. The highest was Gooch ranging from 0.12 to 0.19.

Table 4. Mean absolute error for each of the five GPS-RO techniques.

Technique	Dec-Feb	Mar-May	Jun-Aug	Sept-Nov	Whole Year
Arras	0.08	0.11	0.19	0.11	0.14
Chu	0.07	0.07	0.11	0.08	0.07
Gooch	0.12	0.16	0.13	0.19	0.14
Niu	0.09	0.13	0.12	0.11	0.11
Yu	0.06	0.07	0.10	0.05	0.05

The relative absolute error which shows the performance of a model by using the mean of the absolute value the actual forecast errors divided by the mean of absolute values of the native models' forecast errors (Glen, 2019). The Chu and Yu methodologies have the lowest relative error values at 0.46 and 0.56, respectfully, while the Gooch technique has the largest relative error (Table 5).

Table 5. Relative absolute error for each of the five GPS-RO techniques.

Technique	Dec-Feb	Mar-May	Jun-Aug	Sept-Nov	Whole Year
Arras	0.94	1.05	0.86	1.37	1.35
Chu	0.66	0.59	0.49	0.70	0.46
Gooch	1.43	1.67	0.89	2.59	1.43
Niu	1.04	1.41	0.59	1.28	1.04
Yu	0.61	0.56	0.55	0.49	0.56

The Pearson R correlation or Pearson Product Moment Correlation (PPMC) shows a linear relationship between two sets of data (Glen, 2017). Table 6 shows

that Arras has the strongest correlation during the summer and spring seasons. Yu had the highest value during the fall season with Niu and Chu during the winter.

Table 6. Digisonde and GPS-RO occurrence rate Pearson R correlation coefficients.

Technique	Dec-Feb	Mar-May	Jun-Aug	Sept-Nov	Whole Year
Arras	0.54	0.41	0.72	0.33	0.34
Chu	0.58	0.28	0.67	0.39	0.53
Gooch	0.26	0.07	0.16	-0.34	-0.09
Niu	0.58	0.35	0.67	0.43	0.41
Yu	0.30	0.35	0.64	0.63	0.32

Statistical similarity is calculated as the percentage of overlap between uncertainty intervals calculated for a particular statistical metric. For the occurrence rate means, the statistical similarity is displayed in Table 7. As highlighted by the bootstrapping figures, the Yu technique shows the most overlap and has the strongest statistical similarity with the Digisonde mean over all seasons. Most other techniques show little to no statistical similarity with the Digisonde mean.

Table 7. Digisonde and GPS-RO mean statistical similarity confidence rates.

Technique	Dec-Feb	Mar-May	Jun-Aug	Sept-Nov	Whole Year
Arras	0.01	0.01	0.07	0.02	0.00
Chu	0.00	0.00	0.03	0.04	0.00
Gooch	0.00	0.00	0.75	0.00	0.00
Niu	0.01	0.00	0.51	0.01	0.00
Yu	0.38	0.55	0.84	0.22	0.86

V. Conclusions

Five GPS-RO methods for monitoring sporadic-E from Arras and Wickert (2018), Chu et al. (2014), Niu et al. (2019), Gooch et al. (2020), and Yu et al. (2020) are compared against Digisonde results obtained through the GIRO network to find a technique with strong agreement. Data over a period of 2010-2017 was analyzed and separated by season to compare the techniques' applications and results. Results for the five techniques varied depending on the statistical measurement and season.

The Arras and Wickert (2018) method overestimated throughout most of the comparisons with the Digisonde data. The linear fit of the rates compared to the Digisonde rates provided a slope near one-to-one in the summer season. Statistically, the Arras technique overestimated compared to the other methods, but it had the strongest correlation with Digisonde data for half of the year (two seasons).

The Chu et al. (2014) method underestimated the ratio in almost every Digisonde comparison. However, the linear slope of the trendline was closest to the Digisonde data for the summer months. The Chu method underestimated in the statistical similarity of the mean in each season as well as fall, and was under the rolling average of the Digisonde occurrence rates for each latitude. Statistically, Chu performs better than the other methods when analyzing the relative absolute error and Pearson R correlation. However, differentiating the year into seasons removes that advantage.

The Niu et al. (2019) and Gooch et al. (2020) methods both overestimated the sporadic-E occurrence rates across all metrics. The Gooch method also showed a reduced linear slope for the ratios indicating an overestimation of the low occurrence rate scenarios. Focusing on the mean and median occurrence rates, both methods appeared to track one another due to the reliance on TEC for these methods. Only in the summer months do the two methods overlap the Digisonde confidence interval.

The Yu et al. (2020) method overestimates slightly for the lower occurrence rates

but underestimates slightly for the higher occurrence rates. Through the occurrence ratios the Yu method maintained a close correlation with the Digisonde ratios and the same relationship was observed for the estimates across each latitude. For the mean and median occurrence rates the Yu method falls within the Digisonde confidence interval throughout all seasons. Statistically, the Yu technique outperformed the other methods in mean absolute error, relative absolute error, and mean statistical similarity confidence percentage. While the Yu technique provides a sound estimation of sporadic-E occurrence rates, the linear trendlines with respect to Digisonde rates show that if the ratios were to approach higher values this technique might not outperform the others. In most cases the S4 technique used by Yu showed the closest agreement with the Digisonde measurements during the span of 2010-2017.

The Chu methodology and the use of a weighted linear fit produced a close correlation to the Digisonde results, outperforming the Yu S_4 technique. However, the Chu methodology was too strict to match the magnitudes perfectly. The recommended technique to use for sporadic-E monitoring and studying of sporadic-E climatologies is the S_4 by Yu et al. (2020).

For future research, these methods could be used to create an updated global climatology of sporadic-E occurrence. Combining the GPS-RO data with ionosonde data would provide a powerful combination with nearly global coverage. Possible improvements to the Yu et al. (2020) technique may include the implementation of the L_2 signal in some manner even though it is noisier. Another possible improvement to the Yu et al. (2020) technique could be to incorporate the use of phase since the current usage only involves the amplitude of the L_1 signal.

Bibliography

Ahmad, B. (1999). Accuracy and resolution of atmospheric profiles obtained from radio occultation measurements. *Ph. D. Thesis*, page 1647.

Analysis, C. C. D. and Center, A. (2021). CDAAC Homepage. `https://cdaac-www.cosmic.ucar.edu/`. [Online; accessed 9-Jan-2021].

Arras, C. and Wickert, J. (2018). Estimation of ionospheric sporadic e intensities from gps radio occultation measurements. *Journal of Atmospheric and Solar-Terrestrial Physics*, 171:60 – 63. Vertical Coupling in the Atmosphere-Ionosphere System: Recent Progress.

Barona Mendoza, J. J., Quiroga Ruiz, C. F., and Pinedo Jaramillo, C. R. (2017). Implementation of an electronic ionosonde to monitor the earth's ionosphere via a projected column through usrp. *Sensors (Basel, Switzerland)*, 17(5).

Bibl, K. and Reinisch, B. W. (1978). The universal digital ionosonde. *Radio Science*, 13(3):519–530.

Botchkarev, A. (2018). Performance metrics (error measures) in machine learning regression, forecasting and prognostics: Properties and typology. *arXiv preprint arXiv:1809.03006*.

Briggs, B. and Parkin, I. (1963). On the variation of radio star and satellite scintillations with zenith angle. *Journal of Atmospheric and Terrestrial Physics*, 25(6):339–366.

Brownlee, J. (2019). A gentle introduction to the bootstrap method. https://machinelearningmastery.com/a-gentle-introduction-to-the-bootstrap-method/. [Online; accessed 25-Feb-2021].

Cathey, E. H. (1969). Some midlatitude sporadic-E results from the Explorer 20 satellite. *Journal of Geophysical Research*, 74(9):2240–2247.

Chu, Y.-H., Su, C.-L., and Ko, H.-T. (2010). A global survey of cosmic ionospheric peak electron density and its height: A comparison with ground-based ionosonde measurements. *Advances in Space Research*, 46(4):431–439.

Chu, Y.-H., Wang, C., Wu, K., Chen, K., Tzeng, K., Su, C.-L., Feng, W., and Plane, J. (2014). Morphology of sporadic E layer retrieved from COSMIC GPS radio occultation measurements: Wind shear theory examination. *Journal of Geophysical Research: Space Physics*, 119(3):2117–2136.

Chytil, B. (1967). The distribution of amplitude scintillation and the conversion of scintillation indices. *Journal of Atmospheric and Terrestrial Physics*, 29(9):1175–1177.

Community, A. (2021). The Astropy Project Homepage. `https://www.astropy.org/`. [Online; accessed 9-Jan-2021].

Denardini, C. M., Resende, L. C. A., Moro, J., and Chen, S. S. (2016). Occurrence of the blanketing sporadic E layer during the recovery phase of the October 2003 superstorm. *Earth, Planets and Space*, 68(1):1–9.

Fabrizio, G. (2014). Geolocation of HF skywave radar signals using multipath in an unknown ionosphere. In *2014 IEEE Radar Conference*, pages 0422–0425.

Fabrizio, G. (2014). Geolocation of HF skywave radar signals using multipath in an unknown ionosphere. *2014 IEEE Radar Conference*, pages 0422–0425.

Galkin, I. A. and Reinisch, B. W. (2008). The new artist 5 for all digisondes. *Ionosonde Network Advisory Group Bulletin*, 69(8):1–8.

GIRO (2018). All operating and upcoming GIRO sites. `http://giro.uml.edu/`. [Online; accessed 30-Dec-2020].

Glen, S. (2017). Correlation Coefficient: Simple Definition, Formula, Easy Steps. `https://www.statisticshowto.com/probability-and-statistics/correlation-coefficient-formula/`. [Online; accessed 9-Jan-2021].

Glen, S. (2019). Relative Absolute Error. `https://www.statisticshowto.com/relative-absolute-error/`. [Online; accessed 9-Jan-2021].

Gooch, J. Y., Colman, J. J., Nava, O. A., and Emmons, D. J. (2020). Global ionosonde and GPS radio occultation sporadic-E intensity and height comparison. *Journal of Atmospheric and Solar-Terrestrial Physics*, 199:105200.

Gordon, W. E. (1958). Incoherent scattering of radio waves by free electrons with applications to space exploration by radar. *Proceedings of the IRE*, 46(11):1824–1829.

Hajj, G. A. and Romans, L. J. (1998). Ionospheric electron density profiles obtained with the Global Positioning System: Results from the GPS/MET experiment. *Radio Science*, 33(1):175–190.

Haldoupis, C. (2011). A tutorial review on sporadic E layers. *Aeronomy of the Earth's Atmosphere and Ionosphere*, pages 381–394.

Haldoupis, C. (2019). An Improved Ionosonde-Based Parameter to Assess Sporadic E Layer Intensities: A Simple Idea and an Algorithm. *Journal of Geophysical Research: Space Physics*, 124(3):2127–2134.

Haldoupis, C., Pancheva, D., Singer, W., Meek, C., and MacDougall, J. (2007). An explanation for the seasonal dependence of midlatitude sporadic E layers. *Journal of Geophysical Research: Space Physics*, 112(A6).

Hargreaves, J. K. (1992). *The solar-terrestrial environment: an introduction to geospace-the science of the terrestrial upper atmosphere, ionosphere, and magnetosphere.* Cambridge university press.

Headrick, J. M. and Skolnik, M. I. (1974). Over-the-horizon radar in the HF band. *Proceedings of the IEEE*, 62(6):664–673.

Igarashi, K., Nakamura, M., Wilkinson, P., Wu, J., Pavelyev, A., Wickert, J., et al. (2001). Global sounding of sporadic E layers by the GPS/MET radio occultation experiment. *Journal of Atmospheric and Solar-Terrestrial Physics*, 63(18):1973–1980.

Komjathy, A., Sparks, L., Wilson, B. D., and Mannucci, A. J. (2005). Automated daily processing of more than 1000 ground-based GPS receivers for studying intense ionospheric storms. *Radio Science*, 40(06):1–11.

Kursinski, E., Hajj, G., Schofield, J., Linfield, R., and Hardy, K. R. (1997). Observing earth's atmosphere with radio occultation measurements using the global positioning system. *Journal of Geophysical Research: Atmospheres*, 102(D19):23429–23465.

Kursinski, E. R., Hajj, G. A., Leroy, S. S., and Herman, B. (2000). The GPS radio occulation technique.

Niu, J., Weng, L., Meng, X., and Fang, H. (2019). Morphology of Ionospheric Sporadic E Layer Intensity Based on COSMIC Occultation Data in the Midlatitude and Low-Latitude Regions. *Journal of Geophysical Research: Space Physics*, 124(6):4796–4808.

Observatory, M. H. (2018). Millstone Hill Incoherent Scatter Radar. `https://www.haystack.mit.edu/about/haystack-telescopes-and-facilities/millstone-hill-incoherent-scatter-radar/`. [Online; accessed 6-Jan-2021].

Reddy, C. and Mukunda Rao, M. (1968). On the physical significance of the Es parameters fbEs, fEs, and foEs. *Journal of Geophysical Research*, 73(1):215–224.

Reinisch, B. (2019). IONOSONDES and the measurements they make. International Reference Ionosphere 2019 Workshop, Frederick University, Nicosia, Cyprus, 2-13 September 2019.

Reinisch, B. W., Galkin, I. A., Khmyrov, G. M., Kozlov, A. V., Bibl, K., Lisysyan, I. A., Cheney, G. P., Huang, X., Kitrosser, D. F., Paznukhov, V. V., Luo, Y., Jones, W., Stelmash, S., Hamel, R., and Grochmal, J. (2009). New digisonde for research and monitoring applications. *Radio Science*, 44(01):1–15.

Resources, S. E. O. (2014). FormoSat-3 / COSMIC (Constellation Observing System for Meteorology, Ionosphere and Climate). `https://directory.eoportal.org/web/eoportal/satellite-missions/content/-/article/formosat-3`. [Online; accessed 6-Jan-2021].

Rice, D., Sojka, J., Eccles, J., Raitt, J., Brady, J., and Hunsucker, R. (2011). First results of mapping sporadic E with a passive observing network. *Space Weather*, 9(12).

Rocken, C., Ying-Hwa, K., Schreiner, W. S., Hunt, D., Sokolovskiy, S., and Mc-Cormick, C. (2000). Cosmic system description. *Terrestrial Atmospheric and Oceanic Sciences*, 11(1):21–52.

Satellite, N. E. and Service, D. (2020). COSMIC 2. `https://www.nesdis.noaa.gov/COSMIC-2`. [Online; accessed 9-Jan-2021].

Schreiner, W. S., Sokolovskiy, S. V., Rocken, C., and Hunt, D. C. (1999). Analysis and validation of GPS/MET radio occultation data in the ionosphere. *Radio Science*, 34(4):949–966.

Smith, E. K. (1957). *Worldwide occurrence of sporadic E.*, volume 582. US Department of Commerce, National Bureau of Standards.

Ware, R., Fulker, D., Stein, S., Anderson, D., Avery, S., Clark, R., Droegemeir, K., Kuettner, J., Minster, B., and Sorooshian, S. (2000). SuomiNet: A Real–Time National GPS Network for Atmospheric Research and Education. 81:677–694.

Whitehead, J. (1989). Recent work on mid-latitude and equatorial sporadic-E. *Journal of Atmospheric and Terrestrial Physics*, 51(5):401–424.

Willmott, C. J. and Matsuura, K. (2005). Advantages of the mean absolute error (MAE) over the root mean square error (RMSE) in assessing average model performance. *Climate research*, 30(1):79–82.

Yu, B., Scott, C. J., Xue, X., Yue, X., and Dou, X. (2020). Derivation of global ionospheric Sporadic E critical frequency (fo Es) data from the amplitude variations in GPS/GNSS radio occultations. *Royal Society open science*, 7(7):200320.

Zeng, Z. and Sokolovskiy, S. (2010). Effect of sporadic E clouds on GPS radio occultation signals. *Geophysical Research Letters*, 37(18).

REPORT DOCUMENTATION PAGE

1. REPORT DATE (DD–MM–YYYY)	2. REPORT TYPE	3. DATES COVERED (From — To)
26–03–2021	Master's Thesis	Aug 2019 — Mar 2021

4. TITLE AND SUBTITLE	5a. CONTRACT NUMBER
A COMPARISON OF SPORADIC-E OCCURRENCE RATES USING IONOSONDE AND GPS RADIO OCCULTATION MEASUREMENTS	5b. GRANT NUMBER
	5c. PROGRAM ELEMENT NUMBER

6. AUTHOR(S)	5d. PROJECT NUMBER
Carmona Jr, Rodney Alan, 1st Lt, USAF	5e. TASK NUMBER
	5f. WORK UNIT NUMBER

7. PERFORMING ORGANIZATION NAME(S) AND ADDRESS(ES)	8. PERFORMING ORGANIZATION REPORT NUMBER
Air Force Institute of Technology Graduate School of Engineering and Management (AFIT/EN) 2950 Hobson Way WPAFB OH 45433-7765	AFIT-ENP-MS-21-M-108

9. SPONSORING / MONITORING AGENCY NAME(S) AND ADDRESS(ES)	10. SPONSOR/MONITOR'S ACRONYM(S)
Air Force Research Laboratory/Space Vehicles 3550 Aberdeen Avenue SE Kirtland AFB, NM 87117 DSN 263-2936, COMM (505) 853-2936 Email: Eugene.dao@us.af.mil	AFRL/RV
	11. SPONSOR/MONITOR'S REPORT NUMBER(S)

12. DISTRIBUTION / AVAILABILITY STATEMENT

DISTRIBUTION STATEMENT A:
APPROVED FOR PUBLIC RELEASE; DISTRIBUTION UNLIMITED.

13. SUPPLEMENTARY NOTES

14. ABSTRACT

Sporadic-E (E_s) occurrence rates from Global Position Satellite radio occultation (GPS-RO) measurements have shown to vary by nearly an order of magnitude between studies, motivating a comparison with ground-based measurements. In an attempt to find an accurate GPS-RO technique for detecting E_s formation, occurrence rates derived using five previously developed GPS-RO techniques are compared to ionosonde measurements over an eight-year period from 2010-2017. GPS-RO measurements within 170 km of a ionosonde site are used to calculate E_s occurrence rates and compared to the ground-truth ionosonde measurements. Each technique is compared individually for each ionosonde site and then combined to determine the most accurate GPS-RO technique for binary (present or absent) E_s measurements. Overall, the Yu et al. (2020) S4 method showed the closest agreement with ionosonde measurements between 2010-2017 and is the recommended technique for future GPS-RO based E_s climatologies.

15. SUBJECT TERMS

GPS Radio Occultation, Sporadic-E, Ionosphere

16. SECURITY CLASSIFICATION OF:			17. LIMITATION OF ABSTRACT	18. NUMBER OF PAGES	19a. NAME OF RESPONSIBLE PERSON
a. REPORT	b. ABSTRACT	c. THIS PAGE			Maj Daniel J. Emmons, AFIT/ENP
U	U	U	U	73	19b. TELEPHONE NUMBER (include area code) (937) 255-3636, x4571; Daniel.Emmons@afit.edu